



**Politecnico
di Torino**

M.Sc. in Automotive Engineering

Master's Thesis

**Investigating the Effects of the
Post-Impregnation Temperature on the
Properties of Carbon Fiber Towpreg for the
Production of High-Performance
Components in the Automotive Industry**

Candidate:

Ahmad Atef Abdullatef HAMED

Supervisors:

Prof. Monica FERRARIS
Prof. Klaus DRECHSLER
Dr. Youssef MRAIDI

Academic Year 2024/25

Acknowledgement

I would like to take this opportunity to express my profound gratitude to the individuals and institutions that have been instrumental in the completion of my master's thesis.

I am deeply appreciative of my academic supervisor at TUM Prof. Dr.-Ing. Klaus Drechsler, head of the Chair of Carbon Composites, for giving me the opportunity to work on this topic, and my academic supervisor at the Politecnico di Torino Prof. Monica Ferraris, professor of materials science and technology, for her help and support.

Words cannot express my gratitude enough to my instructor Youssef Mraidi for his continuous support and guidance throughout duration of the thesis. I am also grateful to Gabriel Rojas Valenzuela for his guidance during the testing phase of this thesis.

Additionally, This work was supported by ITALDESIGN, and I am grateful for their financial assistance, which enabled me to pursue this research.

My family, especially my parents and my sisters deserve special mention for their unwavering love and encouragement. Your belief in me has been a constant source of inspiration.

Lastly, I want to recognize anyone else who may have contributed in ways both large and small, directly or indirectly, to the completion of this thesis.

Abstract

In recent years, the automotive industry has witnessed a growing trend towards the utilization of carbon fiber reinforced plastics (CFRP) for their exceptional mechanical properties and lightweight characteristics. This shift has driven the need for advanced manufacturing processes to meet the demands of high-performance automotive components. This thesis delves into a crucial aspect of CFRP production—carbon fiber towpreg manufacturing, with a specific focus on the influence of post-impregnation zone (PIZ) temperature.

The research conducted at the Chair of Carbon Composites (LCC), Technical University of Munich, investigates the impact of varying PIZ temperatures on towpreg characteristics. Mechanical properties, including inter-laminar shear stress (ILSS) and curved beam bending tests, indicate a subtle improvement with increasing PIZ temperature, attributed to enhanced impregnation facilitated by reduced resin viscosity. However, size effects in ILSS tests necessitate further analysis, while curved beam bending tests prove valuable for comparing process parameters and evaluating flexural behavior in cylindrical components.

Microscopy analysis reveals higher porosity percentages in cured plates compared to literature values for carbon fiber prepregs. The distribution of porosities in interlaminar and intralaminar regions, along with their relationship to fiber volume fraction (FVC), is explored.

Thermal characterization, employing dynamic and isothermal Differential Scanning Calorimetry (DSC) scans, indicates that rapid production speeds result in low residence time and high cooling rates, preventing significant crosslinking reactions during towpreg production. Two kinetic curing models are developed, enhancing understanding of curing kinetics for different resin systems.

Furthermore, probe tack tests highlight the low tackiness of the Huntsman resin system, necessitating a future investigation with a tackier resin to explore the effect of PIZ temperature on tackiness.

Contents

Acknowledgement	III
Abstract	IV
Table of contents	V
List of Abbreviations	VII
1 Introduction	1
1.1 Motivation	1
1.2 Thesis Scope	2
2 Background & State of the Art	3
2.1 Towpreg	3
2.2 Towpreg Production	3
2.3 Mechanical Characterization	10
2.3.1 Interlaminar Shear Strength Tests	10
2.3.2 Curved Beams Bending	11
2.4 Thermal Characterization	12
2.4.1 Kinetic Curing Models	12
2.4.2 Differential Scanning Calorimetry	14
2.5 Tack Characterization	15
3 Materials and Methods	17
3.1 Materials	17
3.1.1 Fibers and Resin Systems	17
3.1.2 Towpreg Spools	18
3.2 Mechanical Characterization	19
3.2.1 Plates & Cylinders Preparation	19
3.2.2 Interlaminar Shear Strength Test	21
3.2.3 Curved Beam 3-Point Bending Test	22
3.3 Micrograph Analysis	24
3.4 Differential Scanning Calorimetry	25
3.4.1 Heat of Reaction, DoC, & Rate of Reaction	26
3.4.2 Kinetic Curing Models	27
3.5 Tack Characterization	29

4	Results & Discussion	31
4.1	Mechanical Characterization	31
4.1.1	Interlaminar Shear Stress Test	31
4.1.2	Curved Beam Bending Test	34
4.2	Micrograph Analysis	36
4.2.1	Porosity & Cured Fiber Volume Content Analysis	36
4.2.2	Microstructure Analysis	37
4.3	Thermal Characterization	39
4.3.1	Differential Scanning Calorimetry Measurements	39
4.3.2	Kamal & Sourour's Model	41
4.3.3	Bailleul's Model	43
4.4	Tack Characterization	45
5	Conclusion	46
	References	48
	List of Figures	55
	List of Tables	56
	Appendix	57
	A	57

List of Abbreviations

Abbreviation	Meaning
AFP	Automated Fiber Placement
CFRP	Carbon fibre reinforced plastic
CTL	Composites Testing Laboratory
DoC	Degree of Cure
DOI	Degree of Impregnation
FVC	Fiber Volume Content
ILSS	Interlaminar Shear Strength
LCC	Lehrstuel fuer Carbon Composites
MIA	Multiple Image Allignment
PIZ	Post-Impregnation Zone
PP	Polypropylene
RMC	Resin Mass Content
UD	Unidirectional
UTM	Universal Testing Machine height

1 Introduction

1.1 Motivation

In recent years, the automotive industry has witnessed a remarkable shift towards the integration of carbon fiber reinforced plastics (CFRP). This dynamic evolution reflects a growing recognition of CFRP's exceptional mechanical properties, lightweight nature, and potential to revolutionize vehicle design, performance, and sustainability standards [25][21].

One of the processes used to manufacture components using CFRP is filament winding. This method involves the winding of continuous fibers, often made of materials like carbon fiber, glass fiber, or other composites, around a mandrel or mold in a precise pattern. Automotive components produced using filament winding include pressure vessels for Hydrogen storage, drive shafts, composite leaf springs, exhaust components, chassis components, and air intake components [61].

The state-of-the-art process used in the industry for filament winding is known as wet-winding (fig. 1.1) [14]. In this process, dry carbon fiber rovings are impregnated with epoxy resin just prior to winding. An alternative to this process is using pre-impregnated fiber rovings called towpreg (fig. 1.2). The use of towpregs is advantageous to the wet-winding process since it can be processed at higher winding speeds and offers more precise control of the resin content resulting in more uniform quality of the produced tanks[23]. This is extremely desirable in the automotive industry in order to meet the ever-increasing demand of higher productivity and better quality.

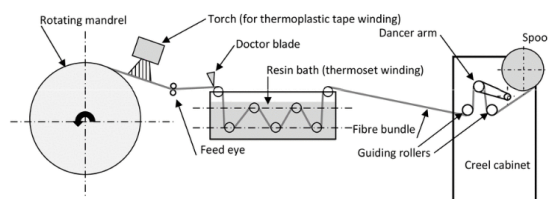


Figure 1.1 : Schematic diagram of the wet winding process [38]



Figure 1.2 : Towpreg winding. Retrieved from TCR Composites

Nevertheless, towpreg production is a complex process which depends on numerous factors; towpreg machines have a large number of parameters to be set, such as machine speed, temperature of resin at impregnation zone, temperatures of rollers and calenders in the post-impregnation zone, temperature of the cooling zone, rewinding pattern, etc..

Thus, understanding the effects of changing these parameters is essential in order to optimize the production process and meet the demands of the industry.

1.2 Thesis Scope

The Chair of Carbon Composites (LCC) at the Technical University of Munich (TUM) acquired recently, from Roth Composites Machinery, a towpreg production machine (fig. 1.3). The machine can impregnate four tows in parallel at process speeds of up to 110 m/min. In addition to the four cross winders, the line has a parallel winder that can produce towpreg with or without release film. The machine contains a heated post-impregnation zone (PIZ), which is made up of a set of heated rollers and calenders, after the impregnation unit.



Figure 1.3 : LCC's towpreg machine

The scope of this thesis is to investigate the effect of the temperature of the heated rollers and calenders in the PIZ of LCC's towpreg machine on the towpreg characteristics. The impregnation in this work is done with thermosetting resins. The effect on the mechanical properties of final parts is examined using inter-laminar shear stress (ILSS) tests and bending tests on curved samples. Furthermore, two kinetic curing models are developed to assess if the rollers' and calenders' temperature causes significant partial curing during the production process. Another important characteristic of towpregs is their tackiness. Probe tack tests are used to evaluate the effect on the tack of the towpregs.

2 Background & State of the Art

2.1 Towpreg

Towpregs are continuous unidirectional fiber bundles (rovings) pre-impregnated with a polymer matrix which are suitable for filament winding processes. They typically consist of carbon fiber or fiberglass filaments impregnated with either thermosetting or thermoplastic resin systems. The pre-impregnation eliminates the need for the impregnation step prior to winding in the wet-winding process [40][41][14].

Utilizing towpreg in filament winding offers distinct benefits over the conventional wet winding technique for specific applications. Towpregs enable finer control over resin content, resulting in reduced variability in mechanical properties once the part is cured and better quality control. Usually, towpreg winding is carried out at higher rates of fiber delivery, leading to increased efficiency in production. The potential for enhanced productivity with towpreg often justifies its higher material expense. Additionally, employing towpreg winding creates a cleaner workspace since, unlike wet winding, towpreg emits minimal volatile offgassing compounds (VOCs) and ozone-depleting compounds (ODCs), ensuring operator safety from hazardous chemicals [23]. However, it's important to mention that towpregs tend to have higher raw material costs compared to wet winding materials. Moreover, they require refrigerated storage and have a relatively limited shelf life at room temperatures. DuVall [23] performed a cost comparison of the production process of CNG tanks using towpreg and wet winding. Although material costs for the towpreg winding process is higher, the profitability during a fixed time period is slightly higher than that of the wet winding process due to the higher throughput.

Towpreg can also be produced for automated fiber placement (AFP) processes. Compared to standard prepregs and slit tapes, it is cheaper and more flexible considering the suitable resin systems. However, its width cannot be consistently regulated with tolerances as narrow as those of slit tapes; instead, it fluctuates in accordance with the width of the roving[40].

2.2 Towpreg Production

In this section, the towpreg production process is discussed, and the towpreg machine at LCC is presented. In addition, some of the practical issues that occur during the production are mentioned. Figure 2.1 shows a schematic diagram of the sections within the towpreg machine. The towpreg production process in general follows the same steps shown in the diagram. However, the production speed is set to 75 m/min, which is

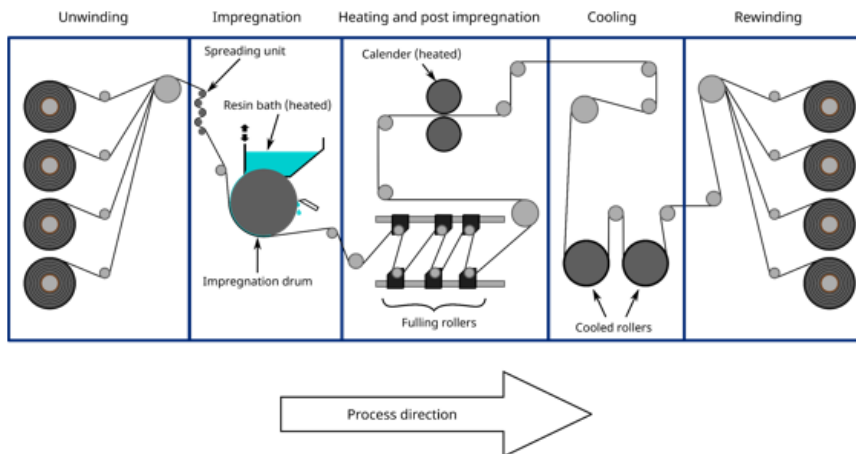


Figure 2.1 : Schematic diagram of the towpreg machine's stages

considerably higher than the state of the art towpreg production systems mentioned in literature [55][66] and other commercially available machines, for instance COMEC Innovative srl [54]¹ and Mikrosam Tow-pregproduction machine².

First, the dry fibers are unwound from the dry fiber spools mounted in the first section of the machine (fig. 2.2). Here, up to four dry spools can be mounted producing four towpreg spools. Other configurations exist such as 6, 8, and up to 16 parallel spools ([54],³). Sensors are installed which monitor the diameter of the mounted spools. When the diameter drops below a specific pre-set value during production, the machine is brought to a halt, and fresh spools are manually installed. A control arm is installed after the spools in order to control the tension in the unwound fibers.



Figure 2.2 : Dry fiber spools unwinding section

¹<https://www.comecinnoative.it/composite/>

²<https://www.mikrosam.com/product/prepreg-making-equipment/>

³See footnote 2

Prior to impregnation, the fibers pass through the spreading unit (fig. 2.3). This consists of five heated metallic rollers which spread the dry fibers preparing them for impregnation. The temperature of this rollers is set to 100°C. Next, the fibers pass through the impregnation unit (fig. 2.3). This unit is made up of a resin bath mounted above a rotating drum. The resin bath is heated such that the viscosity of the resin is controlled during the impregnation process, and its temperature can be set according to the resin system used. A small opening at the bottom of the resin bath allows a thin resin film to flow on the rotating drum where it comes in contact with the dry fibers for impregnation. The size of the opening is the main factor which determines the resin mass content (RMC) of the towpreg. Although the design of this impregnation system is simple compared to other impregnation systems, such as powder deposition systems [55], adjusting the size of the opening is a not. This is because the gap is measured indirectly by a Linear Variable Differential Transformer (LVDT) sensor; the sensor measures the displacement of the moving part that opens and closes the gap. Thus, adjusting the gap size is performed by trial and error. Other factors affecting the FVC include the line speed and resin viscosity. Excess resin is scraped off the impregnation drum, collected, filtered, and subsequently recycled for the impregnation process.



Figure 2.3 : Impregnation unit

Subsequently, the fibers enter the post-impregnation heating zone (PIZ). This consists of seven heated fulling rollers, followed by a bigger heated fulling roller, and finally the towpreg is compacted by a heated calender. The positions of the six smaller fulling rollers are adjustable, and they can even be removed, allowing to change the path of the towpreg in the PIZ. The heating of the rollers allows to partially control the temperature of the towpreg in this zone. Precise control of the tow's temperature is difficult to achieve since the machine is operated at very high speeds which result in extremely low

contact times with the heated rollers and calender and very high cooling by convection. Nevertheless, the tow's temperature governs the resin flow during the production process, which, as a consequence, affects important final towpreg characteristics including tack and degree of impregnation, and final part defects [40]. Furthermore, the heating might also cause a small advancing in the cross-linking reaction of the thermosetting resin systems.

The PIZ consists of a series of rollers of different sizes and a heated calendering unit. 3 types of rollers are present:

- Guide rollers with 4 grooves (fig. 2.5)
- Heated fulling rollers (fig. 2.4)
- Tension measuring rollers

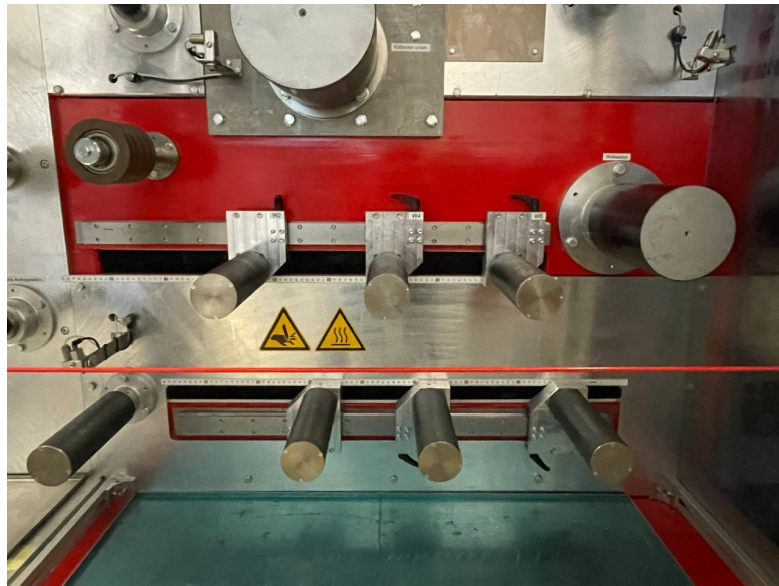


Figure 2.4 : Fulling rollers

In the PIZ, there are 2 guide rollers, 1 tension measuring roller, and a total of 8 heated fulling rollers. The last roller has a larger diameter than the others. The first of the smaller fulling rollers has a fixed position, while the rest of them have a variable position allowing for multiple configurations. Previously, the guide rollers that were installed in the PIZ had a groove width of 7.7 mm. However, since the towpreg width in the PIZ is approximately 5 mm, there was a lot of contact between the towpreg and the grooves' flanges resulting in a high level of fiber damage due to friction. Thus, new guide rollers with groove width equal to 13.3 mm were installed.

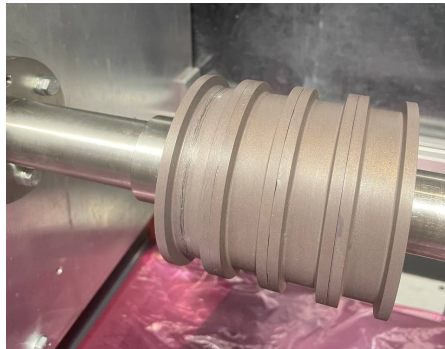


Figure 2.5 : New guide rollers

Currently, the PIZ fulling rollers' and calender's temperature is set to 40°C during production. If the temperature is set any lower, variations of room temperature from summer to winter would affect the production. The maximum available temperature from the machine control is 120°C. However, the practical limit is lower than 100°C since keeping the temperature of the rollers as high as this for long periods of production would result in an increased risk of surface abrasion of the rollers and also the curing of some of the resin that sticks to the rollers during production. This will increase the friction between the rollers' surface and the towpreg causing more fiber damage.

Furthermore, the temperature control of the fulling rollers is carried out by an automatic controller receiving input from an infrared temperature sensor measuring the temperature of the roller at one point of the first fulling roller only. The temperature distribution across the surface of the rollers, nonetheless, is not uniform. This was investigated by taping four thermocouples at four different spots along the length of the roller (fig. 2.6), which would be in contact with the towpregs in case 4 lines are operated simultaneously. Then, the heating of the rollers was switched on and their target temperature was set at 70°C. The measurements from the thermocouples was recorded using PicoLog. Fig. 2.8 shows the measurements of the thermocouples starting from the moment of switching on the heating until the temperature settles. The graph clearly illustrates the non-uniformity of the temperature distribution, showing that the heat source is somewhere between points 3 and 4, where point 4 is the point at the outer end the roller. Moreover, the points closer to the heat source reach temperatures higher than the set temperature, which increases the possibility of causing damage to the rollers and resin curing in these regions due to elevated temperatures. In fact, fig. 2.7 shows the surface of the fulling rollers with visible abrasion after a production run at 100°C. The increased surface roughness will increase the probability of fiber damage.



Figure 2.6 : Thermocouples attached to first fulling roller's surface



Figure 2.7 : Fulling roller surface abrasion

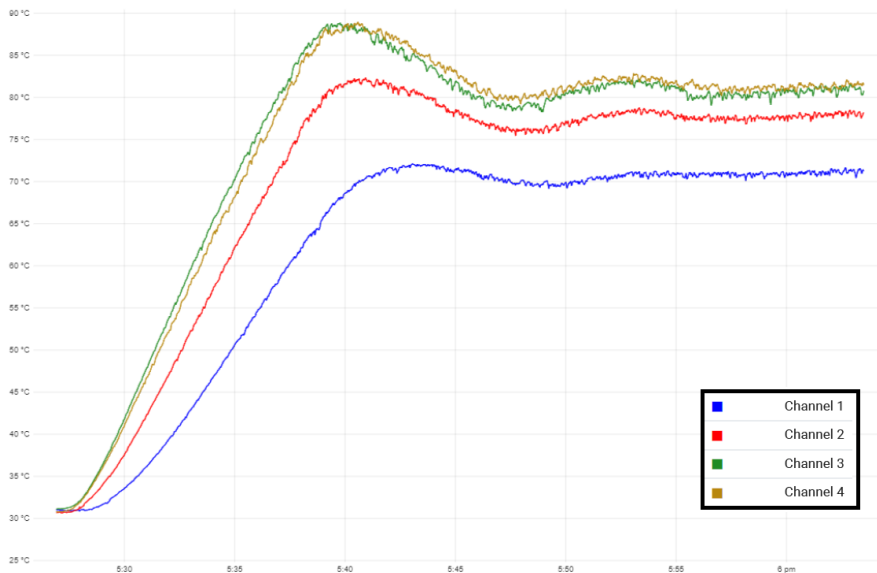


Figure 2.8 : Thermocouples measurements

Next, the towpreg is cooled in the cooling unit (fig. 2.9). This stage marks the end of the impregnation process by lowering the tow's temperature and slowing down the resin flow prior to the rewinding process. The cooling unit contains two large rollers. A problem that occurs in this unit is the condensation of water vapour on the surface of these two rollers, which can cause contamination of the towpreg. In addition, the surface of the rollers becomes more sticky, which causes the towpreg to stick to and wind on the rollers causing the machine to come to a stop. This problem occurs more commonly the higher the PIZ's temperature is, and the lower the cooling unit's temperature is.



Figure 2.9 : Cooling unit

The last step is the rewinding of the towpreg. The LCC's machine contains two winding units:

- 4 cross-winders
- a single parallel-winder



Figure 2.10 : Cross-winders



Figure 2.11 : Parallel-winder

In the cross-winders, only the final feeding rollers are moved along the axis of the fixed, rotating mandrel, while the rest of the winder assembly is stationary. The movement of the feeding rollers causes a lot of distortion and twisting in the towpreg, increasing the friction between the sides of the towpreg and the rollers. As a result, significant fiber damage has been observed on the surfaces of the winders' feeding rollers (fig. 2.12). On the other hand, the feeding rollers of the parallel-winder are fixed while the rotating mandrel moves back and forth. A much lower level of fiber damage has been seen on the surface of the feeding rollers of the parallel-winder w.r.t. the cross-winders. The

parallel-winder also has the possibility of winding with release film. Nevertheless, the use of only one winder, rather than 4 in the case of the cross-winders, during production severely decreases the productivity. Hence, the decision to use one or the other is a compromise between production quality and quantity.



Figure 2.12 : Fiber damage on a cross-winder roller

Altogether, the towpreg production is an intricate process, and its stages depend on many parameters. Hence, each stage requires thorough understanding of the governing parameters in order to optimize the process.

2.3 Mechanical Characterization

Numerous mechanical tests exist for the characterization of mechanical properties of CFRP [27][57][52]. The following two subsections discuss the state of the art of the tests that have been chosen for the present investigation.

2.3.1 Interlaminar Shear Strength Tests

Interlaminar shear strength (ILSS) is defined as the shear stress at which fracture occurs between two layers of a composite laminate, which represents the resistance to delamination [27][57][52]. This is determined using short beam 3-point bending test, which is standardized by ASTM D 2344 [5], DIN EN 2563 [3], and DIN EN 14130 [2]. The test allows the evaluation of the fiber-matrix bonding in a quick and material-efficient manner. The test results are affected by material homogeneity and bulk porosity [63]. In fact, short beam bending tests are used in the industry as a quality control method for these reasons. In the literature, they were used in Celik et al.'s investigation on the influence of the towpreg production process parameters on the mechanical properties [66]. Other examples exist in literature for the mechanical characterization of CFRPs produced using different processes using ILSS tests [7][65][58].

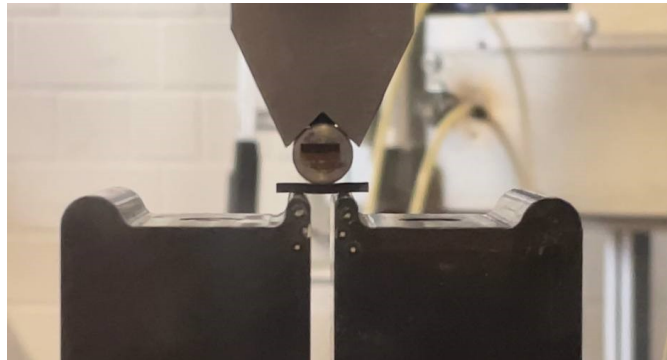


Figure 2.13 : ILSS test setup

2.3.2 Curved Beams Bending

Characterization of the flexural behaviour of CFRPs is carried out using 3- and 4-point bending tests. These tests are standardized for flat samples (ASTM D 790 [4] and DIN EN 14125 [1]), which are cut from unidirectional carbon fiber reinforced polymer (UD-CFRP) plates. The plates can be produced by towpreg winding using a mandrel with 2 flat sides. Consequently, the mandrel is vacuum-bagged and placed in a heated press for the curing at high temperature under pressure, thus producing 2 plates per mandrel (see subsec. 3.2.1). This curing process is completely different from the curing process that is used for cylindrical components such as pressure vessels [35][43], since, in the latter case, no external pressure is applied during the curing process. Subsequently, the former method cannot be used for the mechanical characterization of cylindrical components. A new characterization method is implemented in this study for the comparison between the different PIZ temperatures using 3-point curved beam bending tests, hence, allowing the evaluation the flexural behaviour of components such as pressure vessels [47]. The method and sample dimensions are adapted from DIN EN 14125.



Figure 2.14 : Curved beam bending test setup

2.4 Thermal Characterization

Heat can be supplied to the towpreg in the PIZ by setting elevated roller and calender temperatures. When heat is applied to the thermosetting resins, they cure chemically to form a cross-linked network, becoming rigid, insoluble, and thermally stable [22][20].

Partial curing can occur to the thermosetting matrix of prepreg materials. The partially cured resin state is referred to as the B-stage. The A- and C-stages of resin systems refer to the freshly mixed and fully cured states, respectively. The B-staging process can be tuned so that this state fits to the desired material properties, such as certain level of tack and better drapability [12][8]. The improvement of these properties facilitates the winding and lay-up processes during production. Furthermore, the B-staged material is less susceptible than the uncured resin to moisture absorption, which would cause void formation in the final part. Another advantage of B-staging is the reduction in cure shrinkage due to the reduction in available curing energy in contrast to the uncured resin. On the other hand, advancing the resin to a high degree of cure (DoC) during B-staging would hinder the final curing process, thus, negatively affecting the mechanical properties of the final part. Budelmann et al. [12] refer to other authors who have found that a DoC in the range 20-30% produced the best trade-off between prepreg characteristics. However, the method to obtain this level of DoC is by putting the uncured prepregs in the oven for a specific amount of time and at a controlled temperature after the impregnation process is done. Beck & Colton [8] developed a B-staging line where the towpreg is passed through a heated tunnel oven, but to achieve considerable B-staging, extremely low line speeds were employed. These methods are incompatible with the high throughput rate required by the towpreg industrial standards [54], which makes producing towpregs with this level of DoC impractical.

2.4.1 Kinetic Curing Models

The curing reaction can be characterized by kinetic models which link the rate of reaction to temperature and DoC. These models can be used to understand the extent, if any, to which the cross-linking reactions of the resin matrix proceed in the PIZ. The most commonly used type of curing reaction models are known as phenomenological models [20][9]. These are semi-empirical models which focus on the overall reaction and do not consider the mechanisms of the elementary reactions that occur during the curing process, thus offering simplicity and practicality over the mechanistic curing models. The formulation of these models is based on equating the rate of reaction, expressed as the derivative of the DoC with respect to time, to the product of a rate constant, that is dependent on temperature and defined by an Arrhenius type equation, and a function of the DoC that represents the amount of reacted resin. Thus, knowing the curing temper-

ature and the curing time, it is possible to estimate the DoC using these models. The formulation behind the two models chosen for this study are discussed in this section.

It is important to note that the models presented in this section are intended to give a better understanding of the extent to which cross-linking reactions might occur in the PIZ, and whether or not it is safe to maintain the rollers at a high temperature during the whole production day without having the resin curing on the rollers' surfaces. The testing is done on neat resin samples, not considering the effect of reinforcements, and for a samples with small sizes. In order to predict the exact DoC of the towpreg, thermodynamic and viscosity models coupled with kinetic curing models are needed to describe what happens in the PIZ [13].

Kamal & Sourour's Model

In general, the curing reactions of amine-epoxy resins are often characterized as autocatalytic reactions, i.e. at least one of the reaction products takes part in the cross-linking process, thus influencing the reaction rate [9]. Kamal & Sourour's model is a generalized form of the autocatalytic model in which the initial rate of the reaction might not be equal to zero [34] [59]:

$$\frac{d\alpha}{dt} = (k_1 + k_2\alpha^m)(1 - \alpha)^n \quad (2.1)$$

where α is the DoC, $\frac{d\alpha}{dt}$ is the rate of reaction, $m + n$ is the overall reaction order related to the stoichiometry of the reaction, and k_1 and k_2 are the catalyzed and autocatalyzed reaction rate constants, respectively. The rate constants are dependent on the absolute temperature T (K) dependent and follow the Arrhenius relationship below:

$$k_i(T) = A_i \exp\left(\frac{-E_{ai}}{RT}\right) \quad i = \{1,2\} \quad (2.2)$$

where A is the pre-exponential coefficient (s^{-1}), E_a is the activation energy of the reaction ($Jmol^{-1}$), and R is the ideal gas constant ($8.314 JK^{-1}mol^{-1}$). This well known model has been used for the characterization of many epoxy polymerization reactions [64][26][42], due to its generalized form and relative ease to extract the model parameters from the DSC scans [46].

Bailleul's Model

One drawback to Kamal & Sourour's model is the fact that the number of rate constants is limited to only two. This would become a limitation when the description of more complex crosslinking reactions. A model proposed by Bailleul et al. [33] offers more degrees of freedom, thus allowing to better describe more complex reactions. The main difference between Kamal & Sourour's model and this model lies in the description of the dependence of the rate of reaction $\frac{d\alpha}{dt}$ on the temperature T and the DoC α . The rate of reaction $\frac{d\alpha}{dt}$ is described in the model as the product of two functions:

$$\frac{d\alpha}{dt} = K(T) \cdot G(\alpha) \quad (2.3)$$

$K(T)$ is an Arrhenius function:

$$K(T) = K_{ref} \cdot \exp\left(-B \left(\frac{T_{ref}}{T} - 1\right)\right) \quad (2.4)$$

where T_{ref} is an arbitrarily chosen temperature, K_{ref} is the value of $K(T)$ for $T = T_{ref}$, and B is parameter determined from fitting the model.

On the other hand, $G(\alpha)$ is a polynomial function:

$$G(\alpha) = \sum_{i=0}^n a_i \cdot \alpha^i \quad (2.5)$$

where a_i are the polynomial coefficients and n is the order of the polynomial. The use of the polynomial function gives the model a higher number of degrees of freedom, but the calculations become more involved. The model was used to describe the kinetics of epoxy [6], vinylester, and polyester resins [56][49].

2.4.2 Differential Scanning Calorimetry

The parameters of the kinetic models are obtained using differential scanning calorimetry (DSC) [20][22]. DSC is a widely used tool for thermal analysis for obtaining DoC, glass transition temperature (T_g), specific heat capacity, and/or melting point (T_m) of a material. The DSC measures the heat transferred to or from the material being tested undergoing a physical or chemical reaction. Two operational modes are available for the DSC:

- Isothermal: The temperature is raised very quickly to a certain level and maintained for an extended amount of time. If the sample undergoes a reaction at this temperature, then the heat transfer to/from the sample is recorded until it drops to zero. Using this mode, a graph of the reaction rate against the DoC can be also obtained.
- Dynamic (non-isothermal): The temperature is raised by a set rate starting from a temperature below the T_g of the uncured sample up to a temperature just below its thermal decomposition temperature, while recording the heat transfer. This mode can be used to obtain the total heat of the reaction.

Typically, both methods are used together in the thermal characterization of epoxy resin systems [46]. The parameters necessary for the phenomenological models can be extracted from the results of the DSC runs of both modes.

2.5 Tack Characterization

An important characteristic of towpreg materials is tack. This is the ability of a material's layers to adhere to each other or to a mold surface. The level of tack of prepreg materials should be controlled to facilitate handling and lay-up operations. This is required for the winding and lay-up process of thermoset prepregs in order to inhibit slippage of individual plies and defect generation. Conversely, too much tack is not desirable since incorrectly placed plies cannot be peeled off for correction without being damaged[12][40].

Tack is governed on two opposing mechanisms: the cohesion of the viscoelastic resin and its adhesion to an external surface [11]. The level of tackiness is affected by numerous factors including environment temperature and humidity, resin system, FVC, DoC of the resin, DOI, etc.[40]. Thus, it can be seen that the production process parameters, including the PIZ's temperature, would have a significant effect on the towpreg's tack for a given fiber and resin system. More specifically, the resin flow during the production process would influence the DOI and, consequently, the fraction of resin content on the surface of the towpreg, which in turn decide the resultant level of adhesion of the material when in contact with another surface.

Prepreg tack measurement techniques are derived from tests for pressure sensitive adhesives (PSA). They are often categorized under two major groups: peel tests and probe tack tests [39][62][12]. The former method consists of attaching a strip of the prepreg material to the surface of a metal plate or another strip of the material. Then, the strip is gradually peeled off the substrate while the peeling force is measured. The test is performed using a universal testing machine (UTM), and the pulling angle, pulling rate, and strip width are chosen during the test setup [62]. Using these parameters, the peel-

ing force per unit width of the strip is extracted and used to characterize the material's tack. The main advantage of this method is the similarity with the automatic lay-up techniques. However, some differences exist between the test and the actual lay-up processes. Firstly, the prepreg strip is kept in contact under pressure with the substrate for a long time before peeling relative to the short contact times in actual processes. Moreover, friction between the strip and fiber bending during peeling affect the measured peeling force. Hence, Crossley et al. developed a peel-based tack measurement method involving continuous application-and-peel to account for these issues [17][24]. This method simulates well the AFP process, but as a result the application is mainly restricted to AFP. Heller et al. developed another peel-based method in which, unlike Crossley et al.'s method, the lay-up and peeling rates are uncoupled, and the tack measurement can be carried out at different times after lay-up [30]. Although these developed methods overcome a number of the disadvantages of peel tests, they require specific test fixtures. Peel tests can also be more challenging to observe failure modes and stages than probe tack tests [50].

On the other hand, probe tack tests are easier to implement and do not require tailored equipment. The test is standardized by ASTM D2979 for PSAs, which continues to be used even though it was drawn without replacement in 2019. They have been performed in the past using UTMs and more recently using rheometers [12][10][29]. In a probe test, the prepreg sample is placed on a metal plate and a probe applies a compaction force on the sample for a period of time. The compaction period is followed by a relaxation period, and at the end, the probe is pulled upwards from the sample while the counteracting force and displacement are recorded throughout the duration of the test. The displacement rates and test temperatures are other input parameters. In this test, the prepreg's tackiness is characterized by the value of maximum pull-up force per contact area, which is related to the shear debonding force, and the separation energy, which is the area under the force-displacement curve during the separation phase. This method provides high repeatability and the ability to control precisely the test parameters[12]. Nevertheless, this method does not reproduce the lay-up process conditions. Moreover, the test measures the tack between the prepreg material and the probe, rather than another layer of prepreg, which is the common case during automated lay-up[62]. Furthermore, the test results are sensitive to entrapped air and the sample's surface roughness[17].

3 Materials and Methods

In this chapter, the materials and procedures used to conduct the present investigation are detailed, starting from the fibers, resin systems, and towpreg spools up to the testing methods employed. This serves as the foundation upon which the study's results and conclusions are built.

3.1 Materials

3.1.1 Fibers and Resin Systems

The fibers selected for this investigation are the commercially available Toray T700S-24K-50C, with initial width of 8 mm and filament diameter equal to 7 μm . Two epoxy resin systems are used in this investigation (table 3.1):

- Huntsman
- Hexion

The latter was only used for the thermal characterization.

Table 3.1 : Resin systems used in the investigation

<i>System</i>	<i>Components</i>		
	<i>A</i>	<i>B</i>	<i>C</i>
HUNTSMAN	Araldite LY3508	Aradur 1571	Accelerator 1573
HEXION	Epikote Resin 05910	Curing Agent 05900	Catalyst 05900

3.1.2 Towpreg Spools

In order to investigate the effect of the temperature of the fulling rollers and calenders in the PIZ, the Roth towpreg machine at LCC was used to produce towpreg spools implementing different PIZ temperatures. The lowest PIZ temperature was chosen as 40°C to exclude the effect of the varying room temperatures through the winter and summer seasons. Additionally, the highest practically possible PIZ temperature is 100°C as discussed in section 2.2. An increment of 20°C between chosen temperatures is considered as the best compromise between having very few testing samples, which could not describe well the effect of the PIZ temperature, and too many samples that would be impractical. The chosen temperature values for the study are listed below:

- 40°C
- 60°C
- 80°C
- 100°C

In addition, a towpreg spool was produced with a PIZ temperature equal to 50°C. Furthermore, the produced towpregs are benchmarked against the newly developed commercial Mitsubishi Towpreg¹ with different carbon fibers and resin system.

As discussed in section 2.2, a number of issues arose during the towpreg production process throughout the course of this study, which often caused machine failures bringing the production to a halt. These problems were mainly due to fiber damage. Thus, modifications were introduced to the production configuration and machine parameters to resolve these issues minimizing the number of failures and the amount of fiber damage. The introduced modifications are:

- replacing the old, narrow-grooved guide rollers with newer guide rollers with wider grooves (sec. 2.2)
- using the parallel-winder instead of the cross-winder
- switching off the cooling unit
- the machine speed was reduced due to failures occurring at high speeds when using the parallel-winder

The FVC of the towpreg was measured immediately after each production. The target value of the FVC is 60%. Three samples, approximately 8 m long, were cut from each towpreg spool. Their mass w_s was measured using a balance, and then their length l_s was taken using a 1 m ruler. Next, the FVC was calculated using the following equation:

¹The fibers and resin system of this towpreg are confidential

$$FVC = \frac{\frac{tx}{\rho_f}}{\frac{tx}{\rho_f} + \frac{(\frac{w_s}{l_s} - tx)}{\rho_r}} \quad (3.1)$$

where tx is the fiber's tex, and ρ_f and ρ_r are the densities of the fibers and the Huntsman resin system, respectively. The values of these parameters are reported in table 3.2. Table 3.3 contains all the towpregs used in the present investigation, their average FVC, and the configurations used during their production.

Table 3.2 : Fiber and resin data

<i>Data</i>	<i>Symbol</i>	<i>Value</i>	<i>Unit</i>
Fiber Density	ρ_f	1,76	g/cm ³
Fiber Tex	tx	1650	g/km
Resin Density	ρ_r	1,15	g/cm ³

Table 3.3 : Towpregs used in the investigation

Towpreg	<i>Speed</i> [m/min]	<i>Guide Rollers</i> [new/old]	<i>Winder</i> [pw/cw]	<i>Cooler</i> [on/off]	<i>Towpreg FVC</i> [%]
100°C_OLD	80	new	pw	off	57,44%
100°C_NEW	60	new	pw	off	57,44%
80°C_NEW	75	new	pw	off	59,79%
60°C_NEW	75	new	pw	off	60,88%
40°C_NEW	75	new	pw	off	66,35%
60°C_NEW	80	new	pw	on	55,27%
50°C_OLD	80	old	cw	on	58,48%
40°C_OLD	80	old	cw	on	-

3.2 Mechanical Characterization

3.2.1 Plates & Cylinders Preparation

UD plates and cylinders were prepared using the produced towpregs by filament winding for mechanical testing. The 5-axis CNC winding machine at LCC was utilized. A mandrel with two flat faces was used to wind the plates, while a cylindrical mandrel, 230 mm in diameter, was used to wind the cylinders. Prior to winding, a mould release agent is applied to the surface of the mandrels in order to facilitate the demoulding after curing.

Previously, the towpreg was wound directly on the surface of the mandrel, and the tow tension was 30 N. The plates produced with this older configuration, however, were not

flat and had significant curvature. Thus, a layer of breather and a layer of perforated film are placed on the flat surfaces of the plate mandrel before winding, as shown in figure 3.1. These layers serve as an escape to the gases entrapped between the towpreg and the mandrel. Then, the 5 layers of towpreg are hoop wound on top of the perforated film with a tow tension set to 10 N applied by the winding machine. Next, a layer of peel ply and another layer of breather are placed on top of the towpreg. Finally, the mandrel is placed between two vacuum bag sheets, a small tube is added for the suction of air, and then the vacuum bag sheets are sealed together using tacky tape 3.2. The sealed plate is then put in the press for curing.

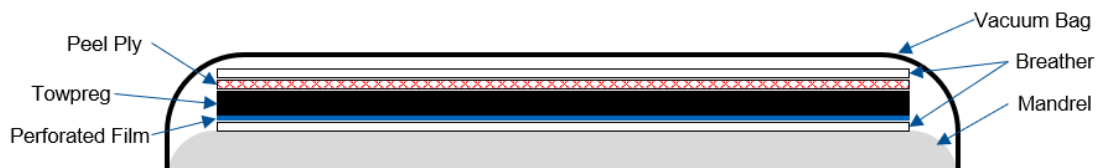


Figure 3.1 : Setup of the vacuum bagging of the plates

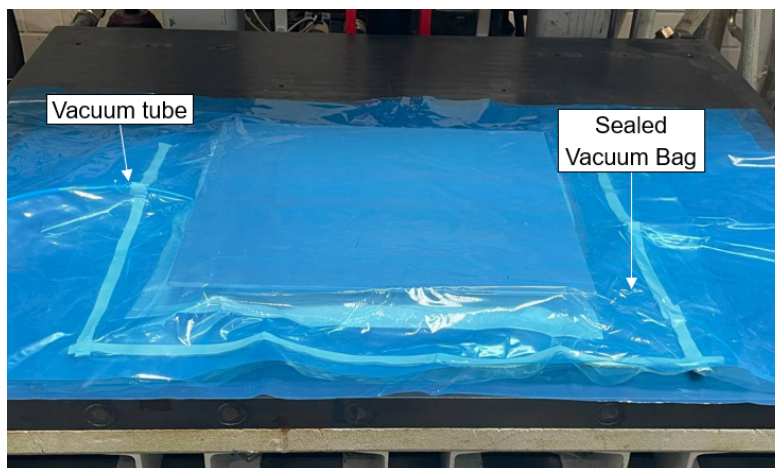


Figure 3.2 : Sealed plate in the press

Before the curing starts, the plate is vacuumed, and the press is lowered. The curing process is done at 2 hours at 100°C, then the temperature is raised to 140°C and maintained for another 2 hours, while the press is applying pressure during the whole process. The vacuuming is stopped after 10 minutes from when the temperature reaches 100°C, since the pressure from the press is enough. At the end of the curing cycle, the heating is switched off, and the temperature is allowed to drop to 30°C before the the press is raised to avoid any residual stresses that might result from high cooling rates if the press would be raised from 140°C. The residual stresses may also cause the plates to have some curvature. Two plates are produced from one mandrel 3.3. Approximately 50 mm are cut from the sides of the obtained plates to avoid regions of irregularities and lower thickness 3.4. These plates are then used to prepare the samples for the ILSS test.



Figure 3.3 : Cured plate

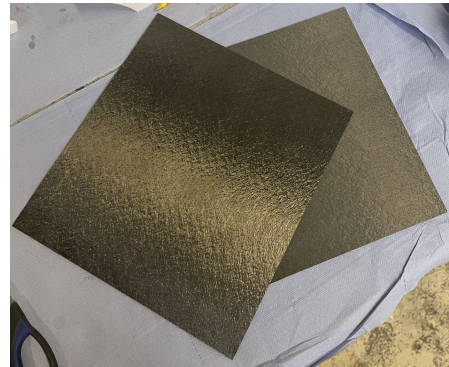


Figure 3.4 : Plates after cutting

In contrast to the plates, 4 layers of towpreg are hoop wound directly on the surface of the cylindrical plate (fig. 3.5). A layer of perforated film and a layer of breather are used to cover the wound towpreg, and then the vacuum bag sheet is added. A small tube for the vacuuming is placed inside the vacuum bag, and then the bag is sealed with tacky tape. Then, the whole mandrel is placed inside the oven and connected to the vacuum machine. After starting the vacuum machine, the curing cycle of 2 hours at 100°C followed by 2 hours at 140°C is applied. The vacuuming is kept on throughout the duration of the curing cycle. The finished cylinder is then cut in rings which are used to make the samples for the curve beam bending test. 4 cylinders were prepared for this investigation using the Mitsubishi Towpreg, 50°C_OLD, 60°C_NEW, and 100°C_NEW towpregs.



Figure 3.5 : Setup of the vacuum bagging of the cylinders



Figure 3.6 : Finished cylinder

3.2.2 Interlaminar Shear Strength Test

The ILSS test samples were prepared following the standard DIN EN 14130[2]. The thickness of the cured plates was around 1.5 mm and, according to the standard, the length and the width depend on the thickness. Thus, the nominal dimensions of the ILSS test samples were 15 mm x 7.5 mm x 1.5 mm. 10 test samples were cut from one of the plates for each chosen PIZ temperature using a cutting machine.

The testing was carried out using the universal testing machine UPM250 at the Composites Testing Laboratory (CTL) at LCC. The testing machine was fitted with a 2.5 kN

load cell. The diameter of the loading nose used was 10 mm, and the diameter of the supports was 4 mm, as recommended by the standard. The loading rate was 1 mm/min. The distance between the support rollers was set equal to 10 mm, deviating from the recommendation of the standard to obtain a better failure mode (see chapter 4).



Figure 3.7 : ILSS test sample

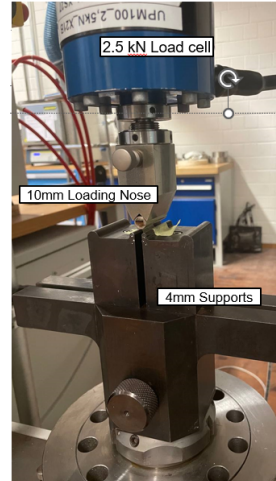


Figure 3.8 : ILSS test setup

Finally, the apparent ILSS τ was calculated for each sample using the following formula:

$$\tau = \frac{3}{4} \cdot \frac{F}{bh} \quad (3.2)$$

where F is the maximum applied load and b and h are the sample's width and thickness, respectively.

3.2.3 Curved Beam 3-Point Bending Test

The dimensions of the samples prepared for the curved were adapted for this test from the standard for the bending of flat samples (DIN EN 14125[1]). The ratios between the thickness, width, and length of the flat samples and the distance between the support rollers were taken as recommended by the standard, but the length was replaced by the arc length of the curved samples. 5 samples were cut from the rings of the cured cylinders by marking the arc length of the samples on the rings before cutting. Only the Mitsubishi, Huntsman 50°C_OLD, 60°C_NEW, and 100°C_NEW cylinders were tested.

The setup used for testing was the same as that of the standard. The support rollers and the loading nose had diameters equal to 4 mm and 10 mm, respectively. The distance between the support rollers was adjusted based on the thickness of the samples. The



Figure 3.9 : Curved beam bending test sample

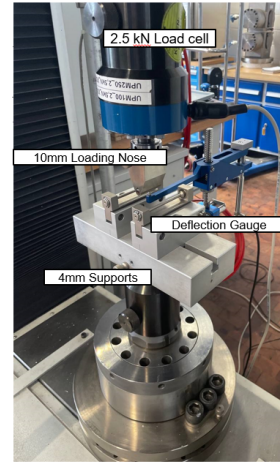


Figure 3.10 : Curved beam bending test setup

tests were done using the same testing machine and load cell used for the ILSS tests, and the loading rate used was 5 mm/min.

The calculation of the bending stress σ_f for each sample was done using the same formula for flat beams:

$$\sigma_f = \frac{3}{2} \cdot \frac{FL}{bh^2} \quad (3.3)$$

where F is the load applied, L is the distance between the support rollers, b is the sample's width, and h is the sample's thickness. This formula was used since the ratio of the radius of curvature of the curved beams and their thickness is very high. The strain was calculated using:

$$\varepsilon_f = 6 \cdot \frac{sh}{L^2} \quad (3.4)$$

where s is the deflection at the middle of the beam. Then, the bending modulus E_f was calculated using the following equation:

$$E_f = \frac{L^3}{4bh^3} \cdot \left(\frac{dF}{ds} \right) \quad (3.5)$$

where $\frac{dF}{ds}$ is the gradient of the load-displacement curve obtained by linear regression of the points between $\varepsilon_f = 0.05\%$ and 0.25% .

3.3 Micrograph Analysis

In order to investigate the microstructure of the cured plates and cylinders, a micrograph analysis was carried out. One microscopy sample per towpreg configuration was cut from a region in the plates close to that of the ILSS samples. The samples were then put in small, 3D-printed plastic cups. Next, an epoxy resin was mixed and degassed before adding it to the cups. The cups were then put in an oven at 40°C and left overnight to cure. After the curing, the bottom side of the cups was polished. The polishing process consisted of sanding using different grit sizes and subsequent diamond-based dispersion polishing.

An Olympus BX41-M microscope was utilized in the analysis for image capturing. The captured images were processed by the Stream Motion software. Firstly, they were converted to black and white for better contrast, and then the thresholds for the pixels were adjusted to calculate the percentage of the area covered by porosity or fibers.

A porosity analysis was conducted on the microscope samples at 10x magnification. 4 pictures were taken along the length of the samples, and the porosity percentage was calculated for each picture. Moreover, a phase analysis was done using multiple image alignment (MIA) technique at 50x to calculate the cured FVC. 3 sets of images were taken along the samples' length. A set of images was consisted of approximately 40 images stitched together. This was done, rather than capturing images of the entire sample, to maintain reasonable image capturing and processing times. The calculation of the FVC was done using 50x magnification because at lower magnification it becomes difficult to distinguish the individual filaments in the images.

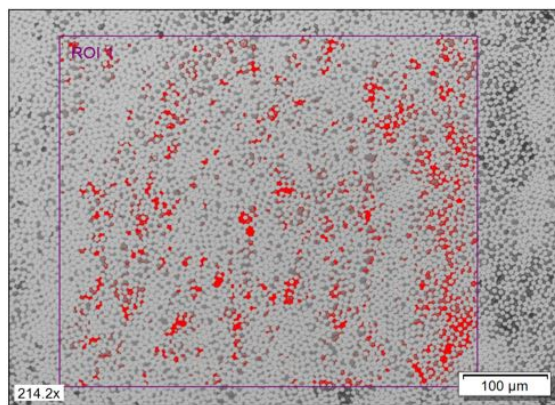


Figure 3.11 : Porosity analysis of a sample from the 100°C_NEW plate

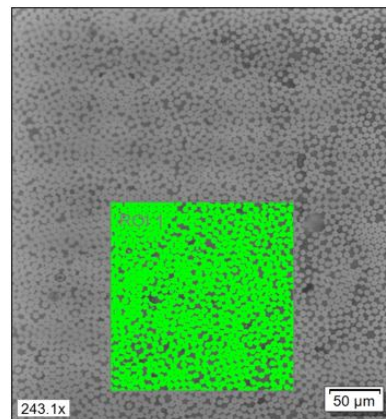


Figure 3.12 : FVC analysis of a sample from the 100°C_NEW plate

3.4 Differential Scanning Calorimetry

A number of DSC measurements were carried out using the dynamic and isothermal modes on uncured samples of the Huntsman and Hexion resin systems (subsection 3.1.1). These measurements were used to extract the parameters of the kinetic curing models chosen for this investigation. All the measurements were carried out using a TA Instruments DSC Q200. Typical resulting graphs obtained from the DSC dynamic and isothermal measurements are shown in figures 3.13 and 3.14, respectively. The samples were prepared by placing one drop of the uncured resin system (weighing approximately between 5-10 mg) in a Tzero Aluminum Hermetic pan and sealed with a Tzero lid. Then the sample and an empty reference pan were put in the DSC.

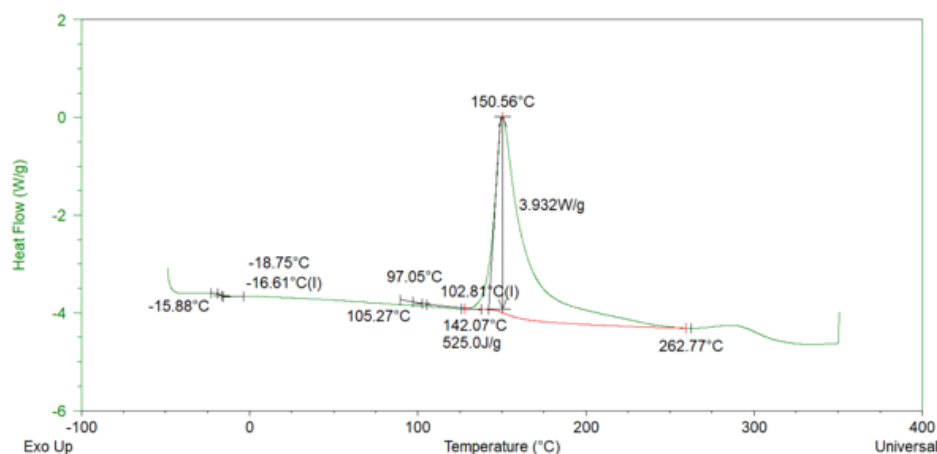


Figure 3.13 : Heat flow vs temperature curve from a DSC dynamic measurement on the Huntsman resin

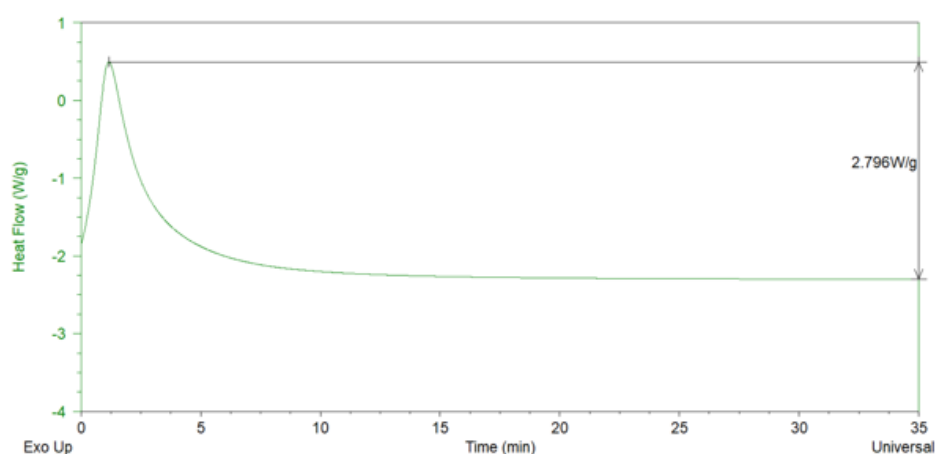


Figure 3.14 : Heat flow vs time curve from a DSC isothermal measurement (140°C) on the Huntsman resin

3 dynamic DSC scans were done for each resin system. Each scan consisted of 2 heating cycles from a starting temperature T_s of -50°C to an end temperature T_f of 350°C for

the Huntsman system and up to 300°C for the Hexion system. The curing occurs during the first heating cycle, while the second cycle was carried out to ensure that the sample fully reacted and measured the cured glass transition temperature T_{gf} . The starting temperature is chosen to be lower than the initial uncured glass transition temperature T_{gi} of the resins [46] [32]. It should be noted that the end temperatures of the dynamic scans were too high. This resulted in a second, smaller exotherm to appear at the end of the first cycle. This was accompanied by a loss in the weight of the samples after the scan is finished, indicating that some decomposition of the sample occurred due to the excessively high temperatures [31]. Thus, the T_{gf} measured during the second cycle is not accurate.

Table 3.4 : DSC dynamic rscan segments

<i>Segment No.</i>	<i>Segment Details</i>
1	Equilibrate at T_s
2	Isothermal for 5.00 min
3	Data storage On
4	Ramp 10.00 °C/min to T_f
5	Isothermal for 1.00 min
6	Mark end of cycle 1
7	Ramp 10.00 °C/min to T_s
8	Isothermal for 1.00 min
9	Mark end of cycle 2
10	Ramp 10.00 °C/min to T_f
11	Mark end of cycle 3
12	Equilibrate at 40.00 °C
13	Data storage Off

Table 3.5 : DSC isothermal scan segments

<i>Segment No.</i>	<i>Segment Details</i>
1	Data storage On
2	Equilibrate at T_{iso}
3	Mark end of cycle 1
4	Isothermal for 120.00 min
5	Mark end of cycle 2
6	Equilibrate at T_{iso}
7	Mark end of cycle 3
8	Data storage Off

After the dynamic scans were completed, 5 isothermal scans were carried out for each system. The isothermal temperatures chosen fall within the range of temperatures situated between a point 10-20°C lower than the onset of the reaction and a temperature positioned halfway to the peak maximum [32]. The selected temperatures for each resin system are listed in table 3.6. Before starting the isothermal runs, the stand-by temperature of the DSC was raised within 10°C, the lid of the DSC was opened, the sample was inserted, and the measurement was quickly started in order to minimize the amount of unrecorded heat released at the start of the measurement [46].

3.4.1 Heat of Reaction, DoC, & Rate of Reaction

The results of the DSC scans are used to calculate the parameters of the kinetic curing models. Firstly, the total heat of the reaction H_{rxn} was calculated using the TA Universal

Table 3.6 : Isothermal temperatures selected for the DSC scans

<i>Resin</i>	<i>Isothermal Temperatures [°C]</i>				
	T_1	T_2	T_3	T_4	T_5
Huntsman	100	110	120	130	140
Hexion	90	100	110	120	130

Analysis software, and it is equal to the area under the exothermal curve obtained from the dynamic scans. The dynamic scans are used rather than the isothermal scans since the samples may not fully react by the end of the isothermal scans [13]. Changes in the baseline of the exothermal curve after curing were observed during the dynamic scans, i.e. the baseline is not a flat line. The changes in the baseline occur due to changes in the specific heat after curing, making the evaluation of the heat of the reaction difficult and less accurate since the baseline definition depends on the operator's judgement and the type of baseline chosen [31]. In the present study, the baseline was defined using the "Integrate Peak Sigmoid Tangent" tool in the TA Universal Analysis software.

Subsequently, a MATLAB script was created to calculate the DoC and the rate of reaction for each isothermal scan. The DoC as a function of time $\alpha(t)$ was calculated using the following equation [46]:

$$\alpha(t) = \frac{\int_0^t \frac{dH}{dt}(t)}{H_{rxn}} \quad (3.6)$$

where dH/dt is the heat flow per unit mass of the resin sample (W/g) measured by the DSC during the isothermal scans. Then, the rate of reaction $d\alpha/dt$ is equal to the derivative in time of the α vs t curve. Next, all the calculated values for each resin system were saved in a structure, which was used to extract the kinetic curing models' parameters.

3.4.2 Kinetic Curing Models

A MATLAB script was written for each model to manipulate the calculated data according to each model's formulation.

Kamal & Sourour's Model

Firstly, the catalysed rate constant k_{1j} in the model's formulation (eq. 2.4.1) was taken equal to the rate of the reaction at the start of the isothermal scan at the temperature T_j :

$$k_{1j} = \left. \frac{d\alpha}{dt}(t = 0) \right|_{T_j} \quad j = \{1, 2, \dots, 5\} \quad (3.7)$$

Next, the model's formulation was fitted to the rate of reaction $d\alpha/dt$ vs DoC α using the non-linear least square fitting method on MATLAB, to obtain k_{2j} , m_j , and n_j from the isothermal scan at temperature T_j . This was then repeated for all the 5 isothermal runs for each resin system. The resulting 5 values of m and n are averaged to obtain the final values of these model parameters.

On the other hand, the parameters of the equation of each rate constant (eq. 2.4.1) A_i and E_i , are obtained by fitting the following equation using linear regression to the k_{ij} vs $1/T_j$ data:

$$\ln(k_i) = \ln(A_i) + \frac{E_i}{R} \cdot \frac{1}{T} \quad i = \{1,2\} \quad (3.8)$$

where A_i and E_i are extracted from the y-intercept and the gradient of the fitted line, respectively.

Bailleul's Model

The calculation of Bailleul's model parameters is more involved. It can be divided into 2 parts:

1. Finding $K(T)$: Firstly, T_{ref} is defined equal to the maximum isothermal temperature. Then, K_{ref} and α^* are defined such that:

$$K_{ref} = \left. \frac{d\alpha}{dt}(\alpha^*) \right|_{T_{ref}} = \max \left(\left. \frac{d\alpha}{dt} \right) \right|_{T_{ref}} \quad (3.9)$$

i.e. K_{ref} is defined as the rate of reaction when the DoC is equal to α^* at the isothermal temperature T_{ref} , which is equal to the maximum rate of reaction recorded during the isothermal scan at the temperature T_{ref} . α^* is defined this way to normalize the function $G(\alpha)$, such that:

$$G(\alpha^*) = 1 \quad (3.10)$$

Next, $\left. \frac{d\alpha}{dt}(\alpha^*) \right|_{T_j}$ is calculated for all the other isothermal temperatures, obtaining 5 values of $\left. \frac{d\alpha}{dt}(\alpha^*) \right|_{T_j}$. The natural logarithm of these values $\ln \left(\left. \frac{d\alpha}{dt}(\alpha^*) \right|_{T_j} \right)$ are plotted against the reciprocals of the isothermal temperatures $\left(\frac{T_{ref}}{T_j} \right) - 1$ where $j = 1, 2, \dots, 5$. Then, the plotted values are fitted with the following logarithmic formula using linear regression:

$$\ln K(T) = \ln K_{ref} + -B \cdot \left(\frac{T_{ref}}{T} - 1 \right) \quad (3.11)$$

However, the following quadratic equation was used instead since it provided better fitting of the data:

$$\ln K(T) = \ln K_{ref} + b \cdot \left(\frac{T_{ref}}{T_j} - 1 \right) + c \cdot \left(\frac{T_{ref}}{T_j} - 1 \right)^2 \quad (3.12)$$

As a result of using the quadratic equation, the modified $K(T)$ equation becomes:

$$K(T) = K_{ref} \cdot \exp \left[b \left(\frac{T_{ref}}{T} - 1 \right) + c \left(\frac{T_{ref}}{T} - 1 \right)^2 \right] \quad (3.13)$$

2. $G(\alpha)$: This function is first calculated using the following formula for each isothermal temperature:

$$G_j(\alpha) = \frac{\frac{d\alpha}{dt} j}{K(T_j)} \quad j = \{1, 2, \dots, 5\} \quad (3.14)$$

Thus, $G(\alpha)$ is not dependent on the isothermal temperature. However, when the linear fitting was used (eq. 1), the curves of $G(\alpha)$ from each isothermal scan were not aligned (fig. 3.15). Thus, the quadratic fitting was used instead which improved the $G(\alpha)$ curves at lower DoC, but the curves are still scattered at higher DoC.

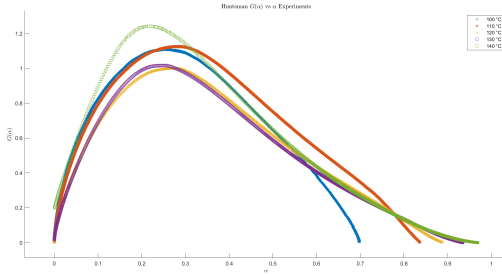


Figure 3.15 : $G(\alpha)$ curves from linear fitting of $K(T)$

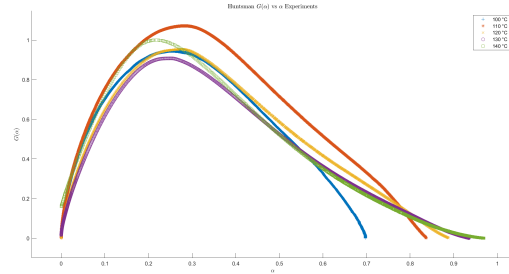


Figure 3.16 : $G(\alpha)$ curves from quadratic fitting of $K(T)$

The resulting 5 curves are then fitted using to a polynomial function of the 7th order, as used in [33], and 5 sets of polynomial coefficients are obtained. Their averages were taken as the final values for defining $G(\alpha)$.

3.5 Tack Characterization

Probe tack tests using the 60°C towpreg spool were conducted in order to assess the level of tack of the Huntsman resin system. The tests were carried out using an Anton Parr MCR 302 rheometer. The overall experimental procedure followed the method

described in Budelmann et al.'s study [10] and Heller et al.'s [29]. The testing parameters are listed in table 3.7. The tests were conducted using a 25 mm diameter probe. 3 pieces of towpreg approximately 15 mm long were cut from the spool and placed carefully side by side under the probe inside the pan of the rheometer (fig. 3.8).

Table 3.7 : Probe tack test parameters

<i>Parameter</i>	<i>Unit</i>	<i>Value</i>
Compaction force	N	20
Compaction time	s	10
Relaxation time	s	5
Temperature	C	20
Displacement rate	mm/s	2

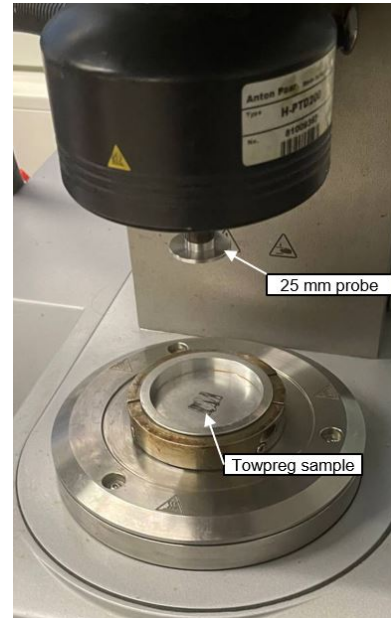


Table 3.8 : Probe tack test setup

After the conclusion of the tests with the 60°C, the resultant level of tack was very low compared to other towpregs previously tested, as will be discussed in section 4.4. Consequently, the other towpreg spools were not tested.

4 Results & Discussion

In this chapter, the results of the mechanical testing, microscopy analysis, kinetic curing models, and tack tests are presented, and the significance of these results is discussed.

4.1 Mechanical Characterization

4.1.1 Interlaminar Shear Stress Test

Figure 4.1 illustrates the results of the ILSS tests. The Mitsubishi Towpreg plate had the highest average apparent ILSS equal to 66.8 MPa, while the 40°C_OLD recorded 46.2 MPa as the lowest value. Among the Huntsman plates, the 100°C_OLD plate had the highest apparent ILSS equal to 57.6 MPa. The average apparent ILSS of the 80°C_NEW plate, 54.6 MPa, was the highest among the newer Huntsman plates. Nevertheless, the Huntsman results are very close and within the standard deviation.

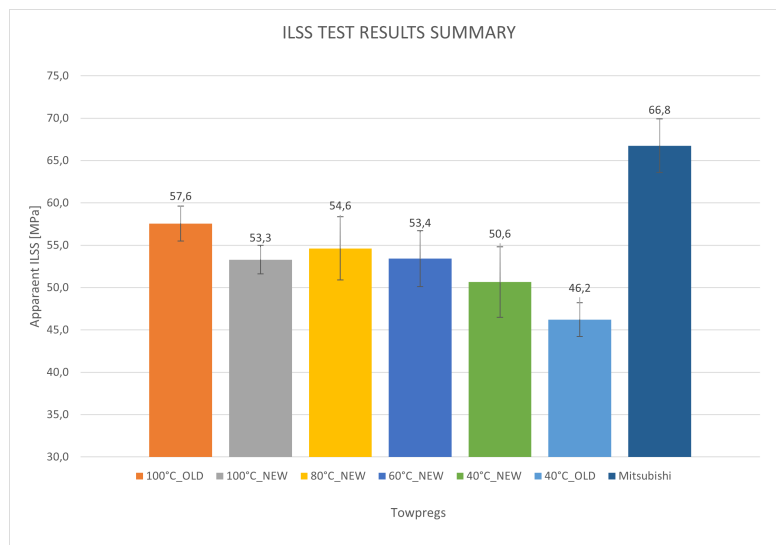


Figure 4.1 : ILSS test results

Discussion

In order to analyze correctly the results, the failure mode should be discussed first. It was previously mentioned (see sec. 3.2.2) that the distance between the support rollers was set equal to 10 mm, deviating from the standard's recommendation. At the start of the testing, the distance used was 7.5 mm as the standard recommends, 5 times the nominal

thickness of the samples. However, the samples tested using this span length inelastically deformed arriving to the so-called compression jamming failure mode, without any delamination [19]. Only pure shear failure is accepted by the standard for measuring the ILSS.

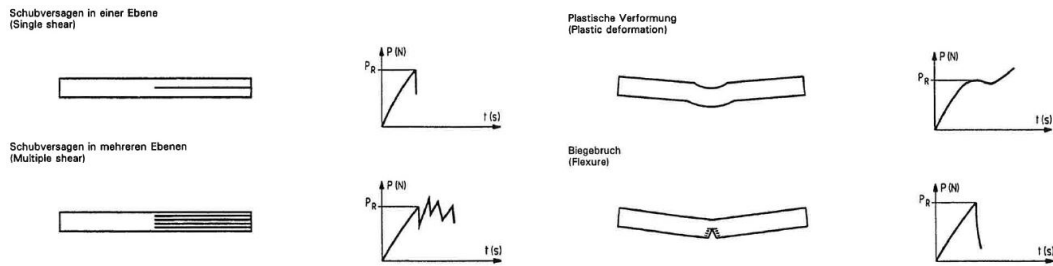


Figure 4.2 : Accepted failure modes by the standards [3]

Figure 4.3 : Rejected failure modes by the standards [3]

The former mode of failure was due to the span being too short. Cui et al. [18] compare the effect of sample size to the failure modes and force-displacement graphs observed during ILSS testing. The smaller samples had a force-displacement curve similar to the ones obtained during testing in this study (fig. 4.5). As a result, the sample gets locked up between the loading nose and the support rollers before any delamination occurs. Hence, the span that was increased to 10 mm instead, which allowed for shear failure to occur, as seen in figure 4.4, and a cracking noise was heard accompanied by sudden drops of the load value during testing [18]. However, the failure was not by pure shear and compressive damage was observed on the surface of the samples in contact with the loading nose, thus the ILSS values obtained are not accepted by the standard. As a result, it is not possible to compare the results of the conducted test obtained from the Huntsman plates and the Mitsubishi Towpreg plate, since the fibers and resin systems are different. It is possible, however, to compare the results of the Huntsman plates, since they are of the same material and all the samples failed in a similar mode.

Although the differences in the ILSS values are not major, the reasons for these differences can be understood by looking at the machine configuration and parameters used in the towpreg production, shown in table 3.3. By comparing the lowest ILSS value recorded by the 40°C_OLD with the ILSS of the 40°C_NEW, it can be seen that the use of the newer wider guide rollers, which caused less fiber damage during production, resulted in better ILSS results.

Moreover, it can be seen the increase in PIZ temperature generally results in an increase in the apparent ILSS, which is possibly attributed to better impregnation resulting from lower viscosity of the resin at higher PIZ temperatures [44]. Figure 4.10 shows the average tow temperatures measured during the production of the towpreg spools using an infrared sensor placed after the calendering unit. Figure 4.7 illustrates the viscosity of the Huntsman resin system from 20°C up to 110°C obtained from a previous investi-

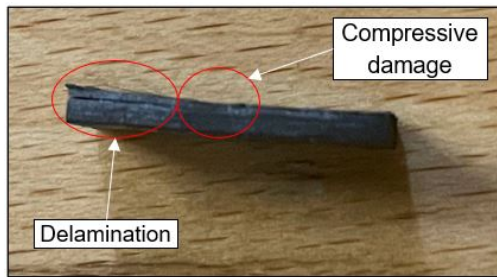


Figure 4.4 : Failure mode from testing (span = 10 mm)

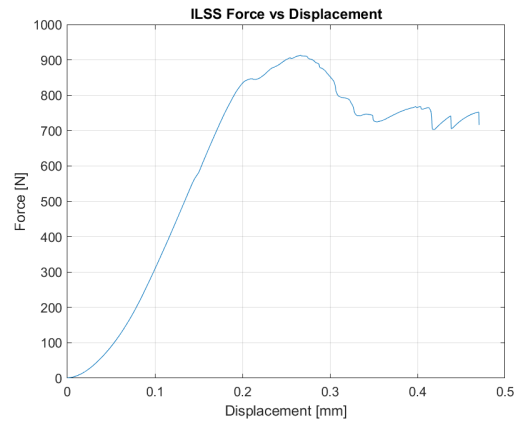


Figure 4.5 : Force-displacement graph of a 60°C_NEW sample (span = 10 mm)

gation, which indicates the extent of the decrease of the viscosity as the temperature increases. In addition, Komkov et al. [37] showed that better impregnation of glass and aramid fibers and lower cured part porosities were obtained by heating the impregnation bath, which reduces the epoxide resin viscosity. In Kim & Lee's paper [36] on impregnation of carbon fibers using polypropylene (PP) films, the ILSS of lower viscosity films was higher at faster impregnation speeds, while the higher viscosity films showed better ILSS only at slower impregnation rates. Thus, the lower viscosities obtained by using higher PIZ temperatures result in better towpreg impregnation, especially in the case of high speed production.

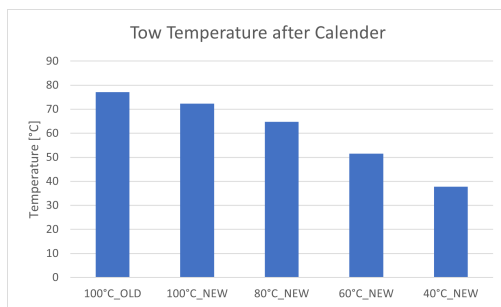


Figure 4.6 : Average tow temperatures after calender

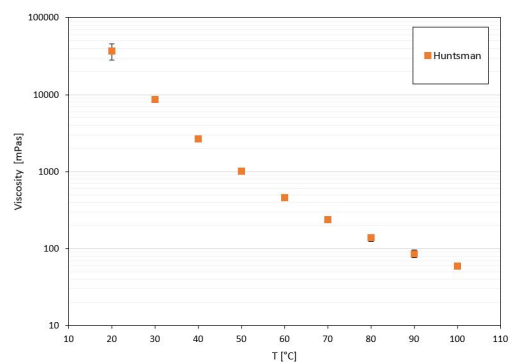


Figure 4.7 : Viscosity of Huntsman resin system

On the other hand, it is difficult to assess with a large degree of certainty the extent of the effect of the decreased resin viscosity in the PIZ on the ILSS. This can be seen in the case of the 100°C_OLD and 100°C_NEW samples. Their production process parameters do not seem to differ significantly, except for their speed, and their tow temperatures after the calendaring unit are similar. Even the effect of the reduced production speed of the 100°C_NEW towpreg should allow better impregnation, in line with the

considerations made in the previous paragraph since a slower speed gives more time for resin flow and impregnation. Thus, the lower ILSS values for the newer spool could be a result of an underlying factor that went unnoticed during production. In addition, it should be noted that the 100°C_NEW towpreg spool was produced at the end of a long production day compared to that of the 100°C_OLD, so it is possible that some resin could have reacted on the surface of the rollers and affected the quality of the spool. For this reason, formulating a conclusive evaluation of the extent of improvement in ILSS is not possible, and further investigation on the repeatability of the process at higher PIZ temperatures is needed.

4.1.2 Curved Beam Bending Test

The results of the curved beam bending tests are summarised in figures 4.8 and 4.9. Overall, all the cylinders had similar strength values within the standard deviation of each other. The 60°C_NEW cylinder had the highest average bending strength just above 1400 MPa, while the 100°C_NEW had the lowest a little less than 1350 MPa. On the other hand, the Mitsubishi Towpreg cylinder had a bending modulus of approximately 90 MPa, which is higher than the Huntsman cylinders. The 100°C_NEW's modulus of 76 MPa was slightly lower than that of the other two at 80 MPa.

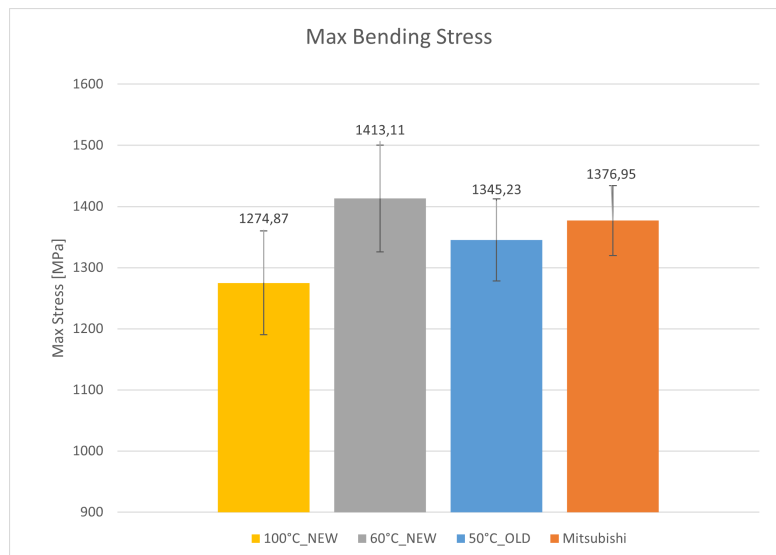


Figure 4.8 : Curved beam bending strength

Discussion

All the samples failed by the same mode, showing the possibility to use the results of this test, not only to compare samples of the same fibers and resin matrix, but also different materials. First, compression failure occurred at the area of the upper surface

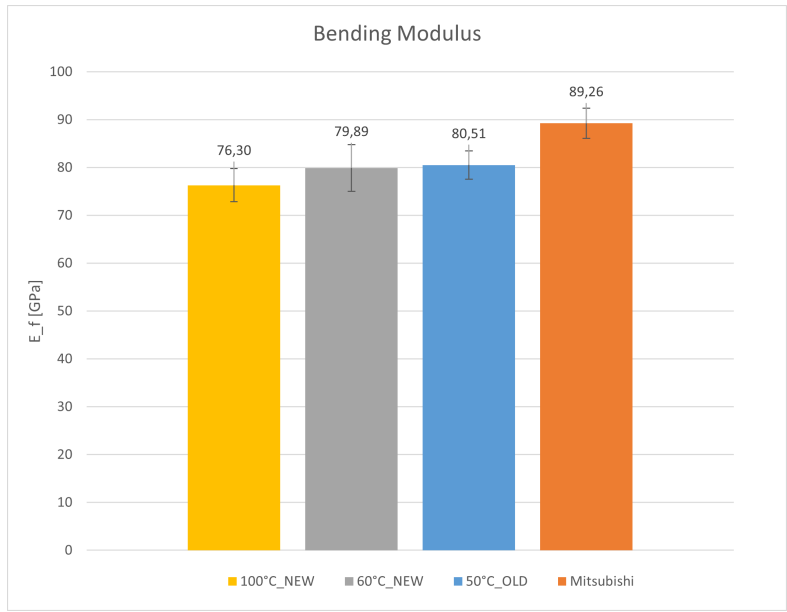


Figure 4.9 : Curved beam bending modulus

of the samples in contact with the loading nose, which was accompanied by small drops in the load and a light cracking noise. Then, delamination occurred, which was followed by a drop in the applied load signaling the end of the test. The delamination occurred at the interface between the laminates at the bottom of the samples, i.e. those under tensile flexural stress. The delamination is dependent on the matrix's toughness [28] and porosity [63] which are affected by the impregnation process. Thus, the curved beam bending test is a good candidate to be used in the characterization of mechanical properties of towpregs.

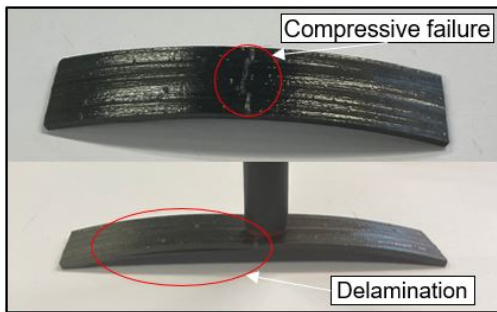


Figure 4.10 : Compressive and delamination failure

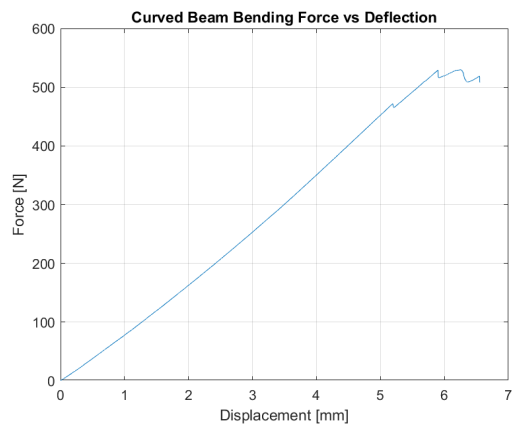


Figure 4.11 : Curved beam bending force-deflection graph

It is not possible to directly compare the results of this test with the ILSS test, due to the curing process by which the samples were produced. Furthermore, it is difficult to compare the trends in the results of both tests because of the fewer number of con-

figurations tested using the curved beam bending test, and the fact that the ILSS were influenced by the size effect of the samples. Nonetheless, similarly to the ILSS test results, the 60°C_NEW cylinder samples had a higher average bending strength than those of the 100°C_NEW. Further testing of the other towpreg configurations, namely the 80°C_NEW, 40°C_NEW, 40°C_OLD, and 100°C_OLD, is needed to have a better understanding of the effect of the process parameters on the curved beam bending test results and to compare and contrast the trends in these results with those of the ILSS test.

4.2 Micrograph Analysis

4.2.1 Porosity & Cured Fiber Volume Content Analysis

The summary of the porosity and cured FVC analysis for the plates is presented in figure 4.12 and 4.13, respectively. The lowest average porosity percentage was recorded by the 60°C_NEW equal to 3.78%, while the highest was 7.1% of the 40°C_NEW. Most of the Huntsman plates recorded higher porosities than the Mitsubishi Towpreg plate. The newer plates had porosity values within the standard deviation of each other. They recorded higher porosity percentages than the 40°C_OLD and 100°C_OLD. On the other hand, the Mitsubishi plate had the highest average cured FVC equal to 67.73%, and the 60°C_NEW and 100°C_OLD showed the lowest two FVC percentages just under 60%. The PIZ does not seem to have a detectable effect on the porosity and the cured FVC.

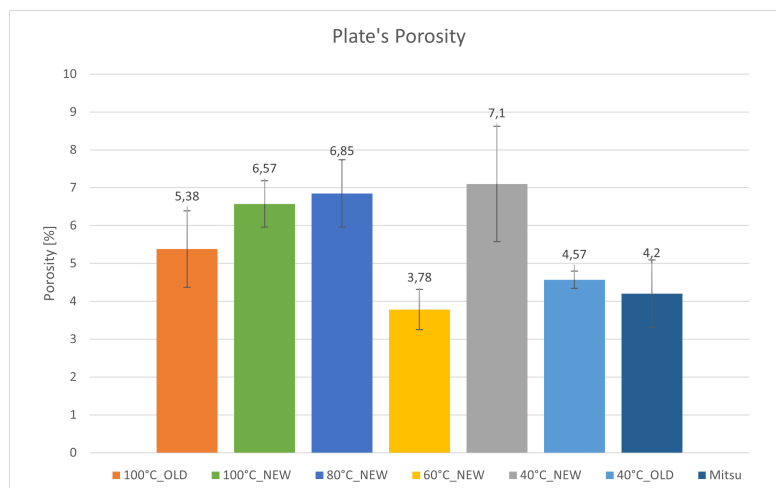


Figure 4.12 : Porosity analysis results

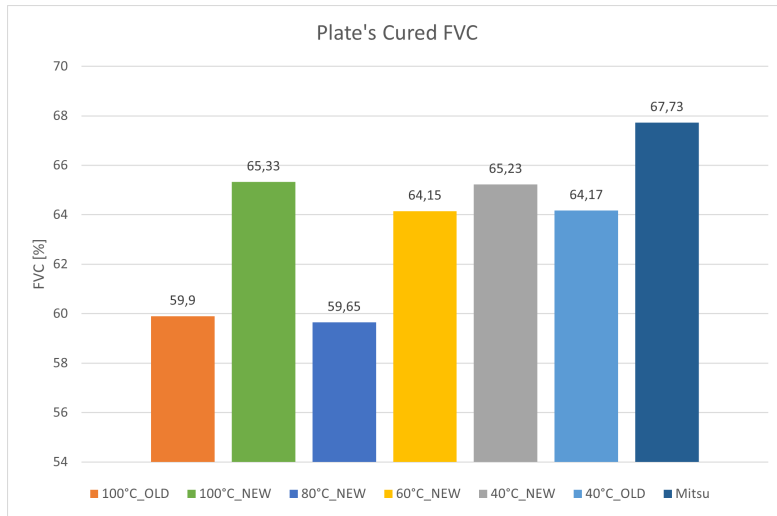


Figure 4.13 : FVC analysis results

Discussion

The porosity percentages obtained are higher than the values reported in literature for prepregs (less than 2% [15] [66]). The increase in porosity in the microstructure causes a decrease in the ILSS [63]. Moreover, most of the FVC percentages not equal to the target FVC after curing of 60% [40]. However, no obvious relationship between the porosity, FVC, and ILSS test results can be deduced from this analysis alone. Although the microscopy samples were cut from a region adjacent to the region from which the ILSS samples were cut, more microscopy samples are needed to describe the porosity and cured FVC more accurately. Furthermore, the definition of the thresholds of the porosity regions and the fibers during image processing (sec. 3.3) is affected by operator subjectivity.

4.2.2 Microstructure Analysis

The inspection of the micrograph images taken of the samples gives some useful insight on the arrangements of the fibers across the materials cross-section and the shapes of the available porosities.

Plates with higher cured FVC had more closely packed fibers, as would be expected. However, the structure is not homogeneous across the entire cross-section of the samples, resulting from non-uniform resin distribution. The regions enclosed by the blue and red ovals in figure 4.14 are regions of closely packed and less tightly packed fibers, respectively, showing a larger resin concentration in the red area.

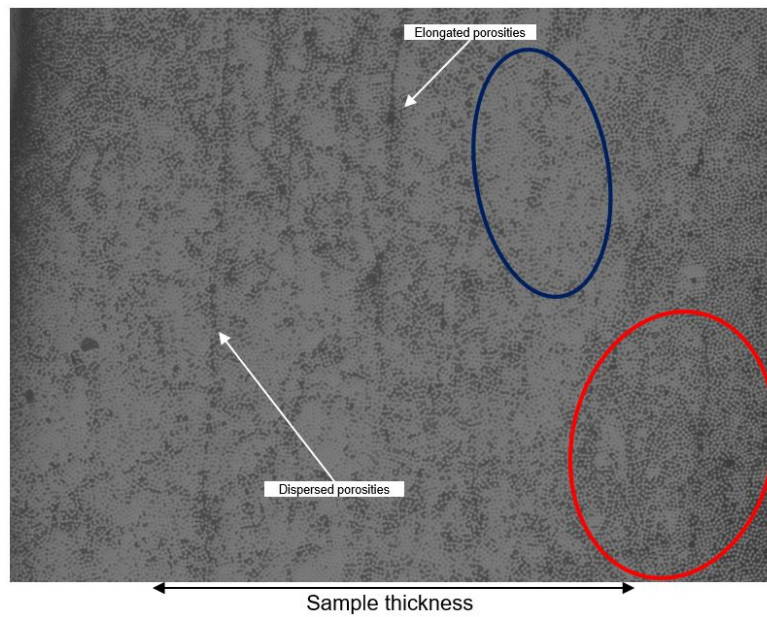


Figure 4.14 : 100°C_OLD micrograph at 5x magnification

From the micrograph images, the porosities can be categorized into two groups, present in all the samples to varying extents, depending on their position in the cross-section [45]:

- Porosities along the interlaminar interface which can be dispersed or connected and elongated (fig. 4.14), and these are responsible for interlaminar failure initiation [63]
- Porosities away from interlaminar regions which are likely to be less common in closely packed fibers regions (e.g. fig. 4.15 shows a more closely packed structure with lower porosity than in fig. 4.16)

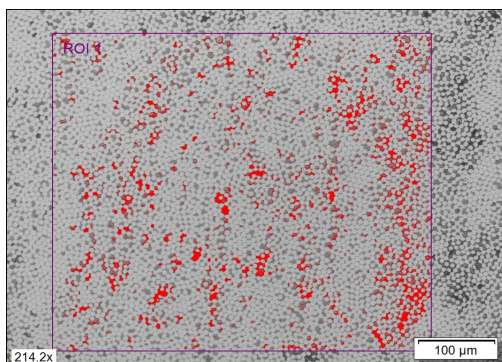


Figure 4.15 : 100°C_NEW micrograph with 5.78% porosity

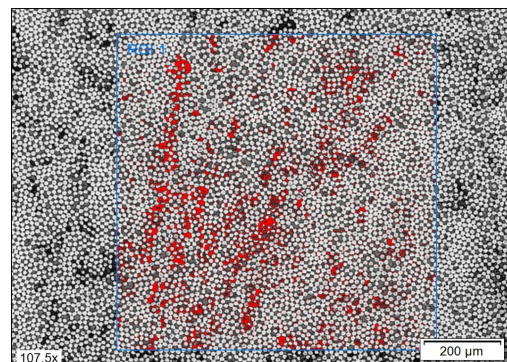


Figure 4.16 : 80°C_NEW micrograph with 8.01% porosity

4.3 Thermal Characterization

In this section, the results of the dynamic and isothermal DSC scans, as well as the kinetic curing models are presented and discussed. The models are then compared to see which one describes more accurately the curing process of the resin systems being examined. Consequently, the extent of partial curing that occurs in the PIZ is discussed.

4.3.1 Differential Scanning Calorimetry Measurements

The results of the dynamic DSC scans are listed in table 4.1. The total heat of reaction H_{rxn} of the Huntsman resin system is equal to 505.5 J/g, higher than that of the Hexion resin system. The reaction of the Huntsman resin system also occurred at higher temperatures, having higher onset and peak heat temperatures.

Table 4.1 : Results of the DSC dynamic scans

<i>Resin System</i>	<i>Extrapolated Onset Temperature</i> [°C]	<i>Peak Heat Flow Temperature</i> [°C]	<i>Peak Heat Flow</i> [W/g]	<i>Total Heat of Reaction</i> [J/g]
Huntsman	142.01 ± 0.45	150.96 ± 0.17	3.941 ± 0.23	505.5 ± 3.12
Hexion	135.36 ± 0.45	146.40 ± 0.51	2.432 ± 0.06	456.27 ± 12.67

The curves $d\alpha/dt$ vs t and α vs t , calculated from the isothermal scans at the 5 different temperatures for both resin systems, are shown in the figures below.

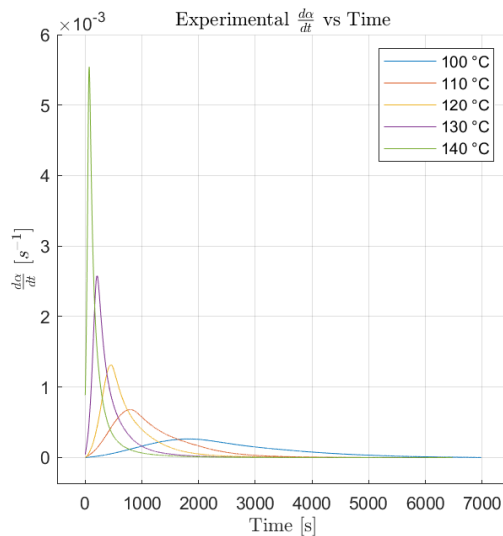


Figure 4.17 : Huntsman $d\alpha/dt$ vs t from experimental results

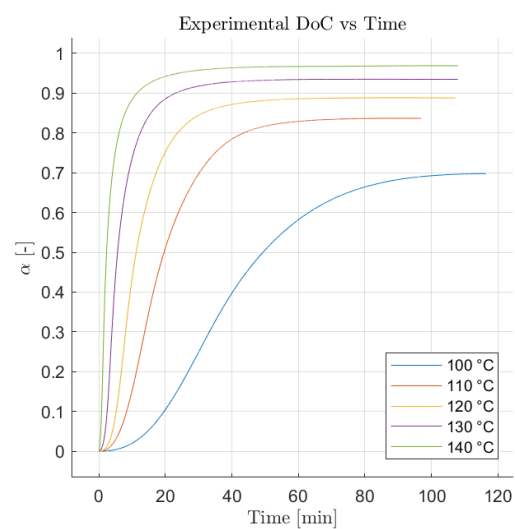


Figure 4.18 : Huntsman α vs t from experimental results

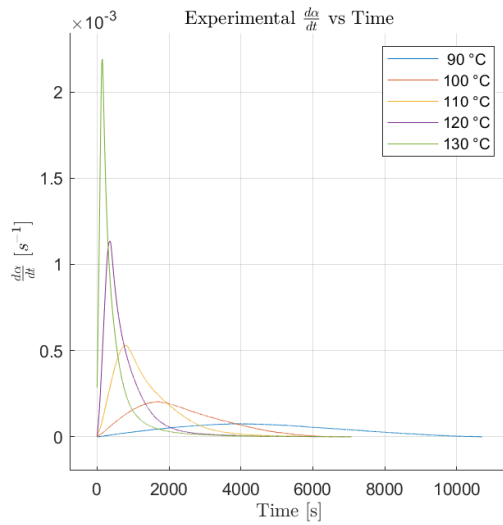


Figure 4.19 : Hexion $d\alpha/dt$ vs t from experimental results

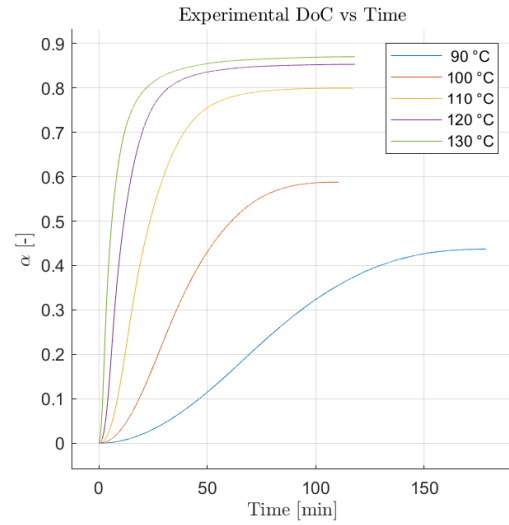


Figure 4.20 : Hexion α vs t from experimental results

Discussion

The values of total heat of reaction H_{rxn} obtained from the dynamic DSC scans for both systems are in good agreement with the range of values in the literature [13] [16] [48] [51]. The graphs of the DoC show that the lower the isothermal temperatures, the lower the maximum DoC that can be reached by the resin at that temperature. The maximum DoC in isothermal conditions depends on how close the isothermal temperature is to the final glass transition temperature T_{gf} [53]. This is the reason for which the total heats of reaction H_{rxn} are often measured using dynamic DSC scans rather than isothermal scans because the sample might not fully react during the isothermal scan.

The reaction The graphs of the rates of reaction $d\alpha/dt$ follow the same trend of other graphs reported in the literature [20]. As the isothermal temperature decreases, the peak of the heat flow from the sample, and consequently the rate of reaction, becomes lower and wider and shifts towards the right since the reaction takes longer to occur.

At 100°C, both resin systems need few minutes in order to achieve significant curing, i.e. DoC in the range 20-30% [12] [8] (fig. 4.18 and 4.20), with the Hexion system requiring more time due less reactivity. This indicates that in the PIZ not a significant amount of crosslinking reactions occur, especially at high impregnation speeds of 75 m/min where the residence time of the towpreg at the elevated temperatures of the PIZ is a few seconds (< 10s). To achieve considerable curing in the PIZ, higher temperatures and slower speeds are needed, which would decrease the productivity and increase the risk of practical issues that would arise due to high PIZ temperatures. However, Huntsman resin system would be a better system to consider to try to achieve a DoC in the range of 20-30% since it has a higher reactivity.

4.3.2 Kamal & Sourour's Model

Table 4.2 summarizes Kamal & Sourour's model parameters obtained from the isothermal results for both resins.

Table 4.2 : Kamal & Sourour's model parameters summary

<i>Resin System</i>	<i>m</i> [-]	<i>n</i> [-]	<i>A</i> ₁ [s ⁻¹]	<i>E</i> ₁ [kJ/mol]	<i>A</i> ₂ [s ⁻¹]	<i>E</i> ₂ [kJ/mol]
Huntsman	0.815	2.554	5.32e+32	287	2.14e+10	93.7
Hexion	0.544	2.492	4.33e+28	254	1.41e+13	117

Discussion

The values for the parameters are in good agreement with those in the literature [13]. Values of around 100 kJ/mol for activation energies are reported in the literature [60] [64] [42], similar to the values obtained in this study. The lower reactivity seen from the Hexion system can also be explained by comparing the activation energies of the two resin systems. The Hexion's higher activation energy means it is more difficult to initiate its curing reaction, than it would be for the Huntsman resin system.

Figures 4.21 and 4.22 report a comparison between the experimental and model predicted α vs t curves at the 5 isothermal temperatures for both resin systems. For both resin systems, Kamal & Sourour's model underestimates the DoC at lower temperatures. For the Huntsman system, the model agrees well with the experimental values at higher temperatures. On the other hand, the model overestimates the DoC for the Hexion system. The underestimation of the DoC is not preferable for the production. This is because a safe temperature predicted by the model may cause curing of the resin.

From these figures, it is also possible to see that the model is unable to predict the final DoC since the model's formulation 2.4.1 considers the resin completely cured ($\alpha = 1$ after the experiment [9]. Some authors proposed modifications to impose a maximum DoC on the model that is dependent on the isothermal temperature [26].

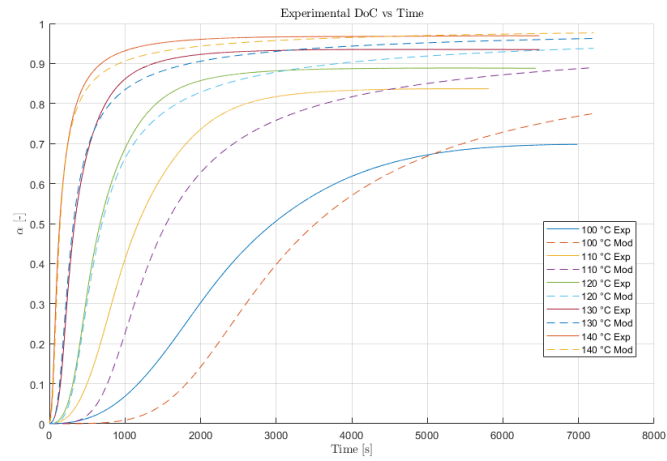


Figure 4.21 : Experimental vs Kamal & Sourour's model predicted DoC for the Huntsman system

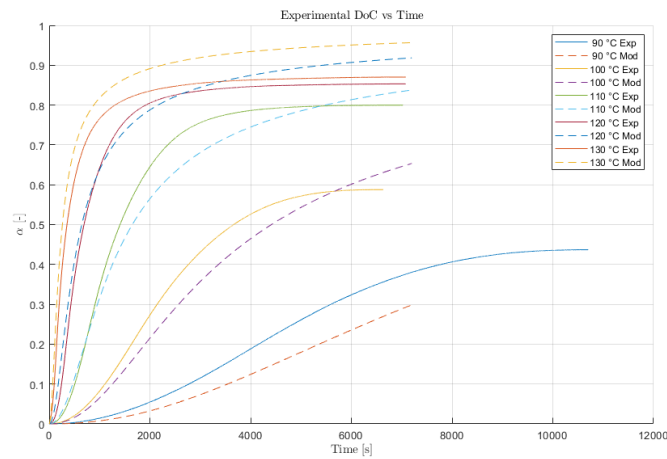


Figure 4.22 : Experimental vs Kamal & Sourour's model predicted DoC for the Hexion system

4.3.3 Bailleul's Model

The parameters for Bailleul's model for both resin systems are listed in table 4.3.

Table 4.3 : Bailleul's model parameters summary

<i>Resin System</i>	T_{ref} [°C]	K_{ref} [s ⁻¹]	b [-]	c [-]
Huntsman	140	0.0055	3.82	-9.06
Hexion	130	0.0022	1.70	-8.48

Discussion

The lower reactivity of the Hexion system is seen in the results since its K_{ref} value is smaller than that of the Huntsman system.

Figures 4.23 and 4.24 show the comparison between the experimental and model predicted α vs t curves at the 5 isothermal temperatures for both resin systems. The model shows very good agreement with the experimental data at low DoC for the Hexion system at all temperatures. Similarly, the model agrees well with the experimental data at low DoC for Huntsman. This is due to the higher number of degrees of freedom of the model.

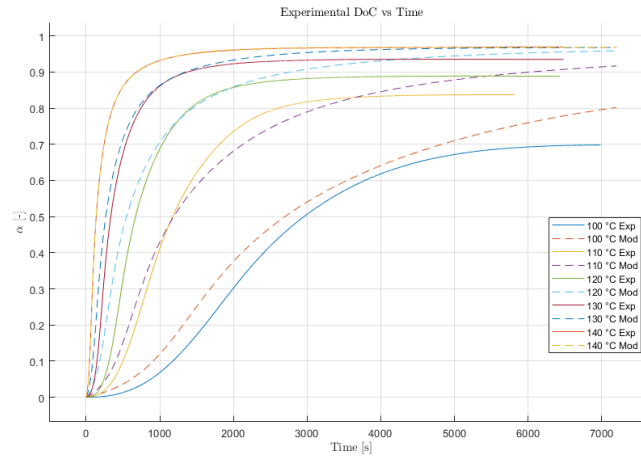


Figure 4.23 : Experimental vs Bailleul's model predicted DoC for the Huntsman system

The problems with the model appear at higher DoC. For the Huntsman system at the isothermal temperatures below 130°C, the model is not able to follow the data at DoC higher than 0.8, and the DoC of the model goes to infinity. In case of the Hexion system, the model deviates starting from around 0.6 DoC. The reason for the failure of the model at higher DoC can be seen from a plot of the function $G(\alpha)$ vs α , shown in figure 4.25.

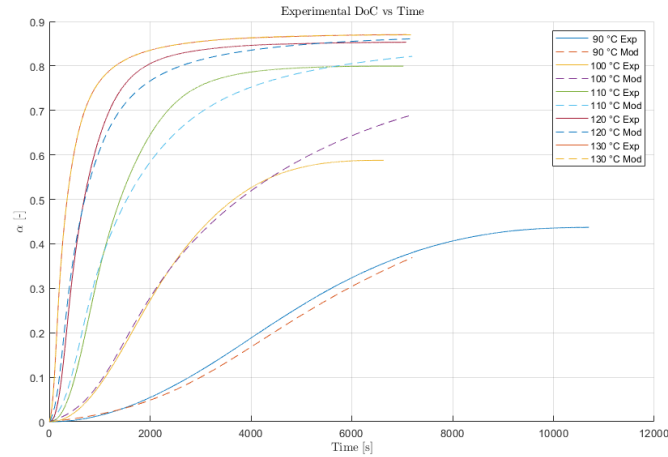


Figure 4.24 : Experimental vs Bailleul's model predicted DoC for the Hexion system

Since $G(\alpha)$ is independent of the temperature, all calculated values of $G(\alpha)$ from the experimental data should be equal. This is the case in the first part of the figure (up to 20% DoC). For higher DoC the values deviate which clearly shows dependence on temperature, thus, the model needs to be modified to accommodate that temperature dependency. Moreover, $G(\alpha)$ becomes negative, which is unrealistic, so the model fails after that point. Some modifications of Bailleul's model can be found in [9].

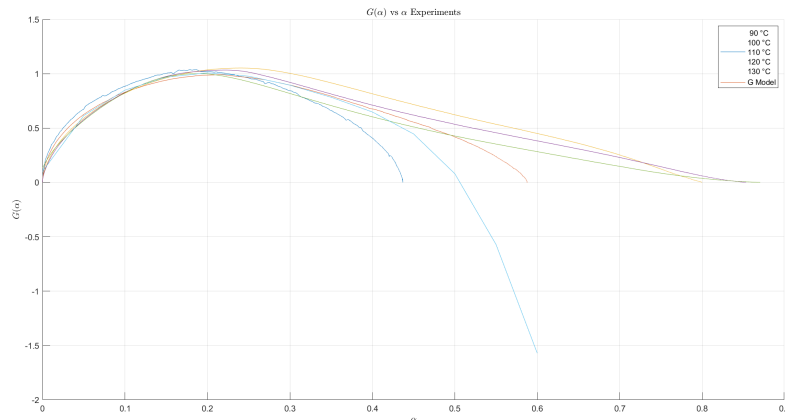


Figure 4.25 : Experimental $G(\alpha)$ function against the $G(\alpha)$ function of the model of Hexion

In contrast with Kamal & Sourour's model, the parameters of this model are empirical so it is difficult to compare with values from investigations on other materials. Regardless, Bailleul's model shows better agreement with the experimental results at lower DoC than Kamal & Sourour's. Thus, it is more suitable for the thermal characterization of the two analyzed resin systems for the towpreg production process, since only partial curing is expected. In addition, it does not greatly underestimate the DoC of the resin unlike Kamal & Sourour's model, so it is better to assess the extent to which the resin might react over the duration of the production day.

4.4 Tack Characterization

The results of the 4 probe tack tests carried out on the 60°C_NEW towpreg at 20°C is listed in table 4.4.

Table 4.4 : Results of the 4 probe tack tests

<i>Test No.</i>	<i>Max. force [N]</i>	<i>Sample length [mm]</i>	<i>Sample width [mm]</i>	<i>Max. force per unit contact area [N/mm²]</i>
1	6,65	15	10	0,0443
2	5,74	14	14	0,0293
3	4,84	15	15	0,0215
4	2,13	14	11	0,0138
Average				0,0272
Std dev				41,4%

Discussion

In a previously conducted probe tack experiment on a commercial SGL Towpreg, the average force per unit contact area at 20°C recorded was 1.92 N/mm². The test was conducted with a 1 mm diameter probe and a compaction force equal to 40 N. Although the parameters of the test are not the same, it can be seen that the level of tack of the Huntsman towpreg is very low. The reason is the low viscosity of the Huntsman resin system (fig. 4.7). This low level of tack, combined with high standard deviation, rendered assessing the effects of the PIZ temperature on the tackiness of the produced towpreg impossible. Further investigation on the PIZ temperatures should be done with tackier resin systems.

5 Conclusion

The effect of the PIZ temperature was studied on the production process, mechanical properties, thermal properties, and tack level of towpregs. The mechanical properties, investigated using mainly ILSS tests and also curved beam bending tests, showed a slight improvement as the PIZ temperature was increased, which was attributed to the improved impregnation due to lower resin viscosity. Although the ILSS test samples were influenced by size effects due to the low thickness of the samples, the results can be used for comparison among towpregs of the same fibers and resin system. The curved beam bending test was proven to be a well suited test for comparing different process parameters and the characterization of the flexural behaviour of cylindrical components, such as pressure vessels. No definitive conclusions about the extent of the effect of the PIZ temperature on the mechanical properties can be drawn from the results of this study yet. Hence, further analysis using matrix-dominated tests, e.g. 90° tensile and bending tests, and conducting more curved beam bending tests on the non-tested towpreg spools is necessary for developing a better understanding of the effect of the PIZ temperature on the mechanical properties.

Moreover, the porosity in microstructure of the cured plates was evaluated using microscopy analysis. The resulting porosity percentages were higher than those reported in the literature for carbon fiber prepregs. The analysis also included the distribution of the porosities at the interlaminar regions and the region inside the laminates. The FVC was also investigated, and its effect on how the fibers are packed was presented. The regions with more closely packed fibers recorded lower porosities. The microstructure of the cylinders is yet to be studied.

Furthermore, DSC was used in the thermal characterization of the Huntsman and Hexion resin systems. Dynamic and isothermal DSC scans were carried out. The isothermal results showed that no significant crosslinking reactions occur during towpreg production due to extremely high speeds resulting in low residence time and high cooling rates. The DSC results were used to develop two kinetic curing models. Bailleul's model was modified to better capture the curing kinetics of the Huntsman system, and good agreement with the experimental results at low DoC was obtained.

Finally, the results of the probe tack tests conducted on the Huntsman resin demonstrated the low tack level of this resin system. Consequently, it was not possible to investigate the effect of the PIZ temperature on the tack level. To do this, the investigation needs to be repeated with a tackier resin system. This is also necessary to understand the sensitivity of different resin systems to changing the PIZ temperature.

Overall, several aspects of towpreg production have been examined in this thesis. The obtained results provided valuable insight into the towpreg production process. These results also act as guidelines for future investigations for the optimization of the towpreg production process.

References

- [1] *DIN EN 14125, Faserverstärkte Kunststoffe - Bestimmung der Biegeeigenschaften*, year = 1997, owner = ga75xiq,.
- [2] *DIN EN 14130, Faserverstärkte Kunststoffe - Bestimmung der scheinbaren interlaminaren Scherfestigkeit nach dem Dreipunktverfahren mit kurzem Balken (ISO 14130:1997); Deutsche Fassung EN ISO 14130:1997*, year = 1997, owner = ga75xiq,.
- [3] *DIN EN 2563, Aerospace Series – Carbon Fibre Reinforced Plastics – Unidirectional Laminates – Determination of Apparent Interlaminar Shear Strength*, year = 1997, owner = ga75xiq,.
- [4] *ASTM D790-17, Standard Test Methods for Flexural Properties of Unreinforced and Reinforced Plastics and Electrical Insulating Materials*, ASTM International, West Conshohocken, PA, 2017.
- [5] *ASTM D2344/D2344M-22, Standard Test Method for Short-Beam Strength of Polymer Matrix Composite Materials and Their Laminates*, ASTM International, West Conshohocken, PA, 2022.
- [6] ABOU MSALLEM, Y., F. JACQUEMIN, N. BOYARD, A. POITOU, D. DE-LAUNAY S. CHATEL: *Material characterization and residual stresses simulation during the manufacturing process of epoxy matrix composites*. Composites Part A: Applied Science and Manufacturing, 41(1):108–115, 2010. Special Issue: Flow Processes in Composite Materials.
- [7] ANANDAN, SUDHARSHAN, GURJOT DHALIWAL, K. CHANDRASHEKHARA, T.R. BERKEL D. PFITZINGER: *Post curing effects on out-of-autoclave BMI composite panels*. International SAMPE Technical Conference, 01 2014.
- [8] BECK, R. W. J. S. COLTON: *A process for prestaging thermosetting towpreg*. Polymer Composites, 20(1):132–145, 1999.
- [9] BOYARD, NICOLAS. John Wiley Sons, 2016.
- [10] BUDELMANN, D., H. DETAMPEL, C. SCHMIDT D. MEINERS: *Interaction of process parameters and material properties with regard to prepreg tack in automated lay-up and draping processes*. Composites Part A: Applied Science and Manufacturing, 117:308–316, 2019.
- [11] BUDELMANN, D., C. SCHMIDT D. MEINERS: *Adhesion-cohesion balance of*

- prepreg tack in thermoset automated fiber placement. Part 1: Adhesion and surface wetting.* Composites Part C: Open Access, 6:100204, 2021.
- [12] BUDELMANN, DENNIS, CARSTEN SCHMIDT DIETER MEINERS: *Prepreg tack: A review of mechanisms, measurement, and manufacturing implication.* Polymer Composites, 41(9):3440–3458, 2020.
- [13] CALADO, VERÔNICA M.A. SURESH G. ADVANI: *Thermoset Resin Cure Kinetics and Rheology*, 32–107.
- [14] CAMPBELL, F. C.: *5.8 Filament Winding*, 2004.
- [15] CENTEA, T., L.K. GRUNENFELDER S.R. NUTT: *A review of out-of-autoclave prepregs – Material properties, process phenomena, and manufacturing considerations.* Composites Part A: Applied Science and Manufacturing, 70:132–154, 2015.
- [16] CHANG, SHU SING: *Heat of reaction and curing of epoxy resin.* Journal of thermal analysis, 34:135–154, 1988.
- [17] CROSSLEY, R.J., P.J. SCHUBEL N.A. WARRIOR: *The experimental determination of prepreg tack and dynamic stiffness.* Composites Part A: Applied Science and Manufacturing, 43(3):423–434, 2012.
- [18] CUI, WEICHENG, MICHAEL R. WISNOM MICHAEL JOHN JONES: *Effect of Specimen Size on Interlaminar Shear Strength of Unidirectional Carbon Fibre Epoxy.* Composites Engineering, 4:299–307, 1994.
- [19] DANIELS, B.K., N.K. HARAKAS R.C. JACKSON: *Short beam shear tests of graphite fiber composites.* Fibre Science and Technology, 3(3):187–208, 1971.
- [20] DAVE, RAJU S., LOOS ALFRED C. Hanser Publishers, 2000.
- [21] DELOGU, M., L. ZANCHI, C.A. DATTILO M. PIERINI: *Innovative composites and hybrid materials for electric vehicles lightweight design in a sustainability perspective.* Materials Today Communications, 13:192–209, 2017.
- [22] DODIUK, HANNA S. GOODMAN: *Handbook of Thermoset Plastics*, 254. 01 2014.
- [23] DUVAL, FREDERICK: *Cost comparisons of wet filament winding versus prepreg filament winding for Type II and Type IV CNG cylinders.* 37, 01 2001.
- [24] ENDRUWEIT, ANDREAS, GABRIEL Y.H. CHOONG, SAYATA GHOSE, BRICE A. JOHNSON, DOUGLAS R. YOUNKIN, NICHOLAS A. WARRIOR DAVIDE S.A. DE FOCATIIS: *Characterisation of tack for uni-directional prepreg tape employing a continuous application-and-peel test method.* Composites Part A: Applied Science and Manufacturing, 114:295–306, 2018.
- [25] FORCELLESE, ARCHIMEDE, MARCO MARCONI, MICHELA SIMONCINI

- ALESSIO VITA: *Life cycle impact assessment of different manufacturing technologies for automotive CFRP components*. Journal of Cleaner Production, 271:122677, 2020.
- [26] GONZÁLEZ-ROMERO, V. M. N. CASILLAS: *Isothermal and temperature programmed kinetic studies of thermosets*. Polymer Engineering & Science, 29(5):295–301, 1989.
- [27] GRELLMANN, WOLFGANG SABINE SEIDLER: *10 - Testing of Composite Materials*. GRELLMANN, WOLFGANG SABINE SEIDLER (): *Polymer Testing (Third Edition)*, 515–567. Hanser, Third Edition , 2022.
- [28] HARRIS, BRYAN: *5 Fracture and Toughness of Composites*, 1999.
- [29] HELLER, KLAUS, DAVID COLIN KLAUS DRECHSLER: *Quantifying the Influence of Out-Time on Prepreg Material Properties and Out-Of-Plane Steering Defects During Automated Fiber Placement*. Frontiers in Materials, 9, 2022.
- [30] HELLER, KLAUS, SIMON SEYFFERTH, KALLE KIND KLAUS DRECHSLER: *A Post Lay-up Tack Peel Test for Aerospace Grade Prepreg Tapes*. 09 2020.
- [31] INSTRUMENTS, TA: *Interpreting Unexpected Events and Transitions in DSC Results*.
- [32] INSTRUMENTS, TA: *A Review of DSC Kinetics Methods*.
- [33] JEAN-LUC, BAILLEUL, DIDIER DELAUNAY YVON JARNY: *Determination of Temperature Variable Properties of Composite Materials: Methodology and Experimental Results*. Journal of Reinforced Plastics and Composites, 15:479–496, 05 1996.
- [34] KAMAL, MUSA R.: *Thermoset characterization for moldability analysis*. Polymer Engineering & Science, 14(3):231–239, 1974.
- [35] KANG, CHAO, YAoyao SHI, BO DENG, TAO YU PENGCHENG SUN: *Determination of Residual Stress and Design of Process Parameters for Composite Cylinder in Filament Winding*. Advances in Materials Science and Engineering, 2018:1–11, 03 2018.
- [36] KIM, JONG WON JOON SEOK LEE: *The effect of the melt viscosity and impregnation of a film on the mechanical properties of thermoplastic composites*. Materials, 9(6):448, 2016.
- [37] KOMKOV, MA, VA TARASOV VM KUZNETSOV: *The influence of epoxide resin viscosity on impregnation of fiber reinforcement*. Polymer Science Series D, 8:292–295, 2015.
- [38] KOUSSIOS, SOTIRIS, L. ZU, C.M. WENTZEL, ADRIAAN BEUKERS MARCEL ELSWIJK: *Filament winding: Process overview novel developments*. International

SAMPE Technical Conference, 01 2012.

- [39] KRÄMER, JOHANNES HAUKE LENGSELD: 7 - *Testing of Prepregs*. LENGSELD, HAUKE, JAVIER LACALLE, THOMAS NEUMEYER VOLKER ALTSTÄDT (:): *Composite Technology (Second Edition)*, 203–216. Hanser, Second Edition , 2021.
- [40] LENGSELD, HAUKE MIKE TURNER: 3 - *Prepreg Technology*, 2021.
- [41] LENGSELD, HAUKE, MAINKAR HENDRIK ALTSTÄDT VOLKER: 5.3.1 *Applications: UD Prepreg (Thermoset)*, 2021.
- [42] LI, QI, XIAOYU LI YAN MENG: *Curing of DGEBA epoxy using a phenol-terminated hyperbranched curing agent: Cure kinetics, gelation, and the TTT cure diagram*. *Thermochimica Acta*, 549:69–80, 12 2012.
- [43] LIU, CHAO YAOYAO SHI: *Design optimization for filament wound cylindrical composite internal pressure vessels considering process-induced residual stresses*. *Composite Structures*, 235:111755, 2020.
- [44] LUTZ, A. T. HARMIA: *Impregnation techniques for fiber bundles or tows*, 301–306. Springer Netherlands, Dordrecht, 1999.
- [45] MEHDIKHANI, MAHOOR, LARISSA GORBATIKH, I. VERPOEST STEPAN LOMOV: *Voids in fiber-reinforced polymer composites: A review on their formation, characteristics, and effects on mechanical performance*. *Journal of Composite Materials*, 53:002199831877215, 11 2018.
- [46] MENCZEL, JOSEPH D., LAWRENCE JUDOVITS, R. BRUCE PRIME, HARVEY E. BAIR, MIKE READING STEVEN SWIER: *Differential Scanning Calorimetry (DSC)*, 2, 7–239. John Wiley Sons, Ltd, 2009.
- [47] MOSS, DENNIS R., BASIC MICHAEL M. Elsevier, 2013.
- [48] NAM, JAE-DO JAMES C. SEFERIS: *Application of the kinetic composite methodology to autocatalytic-type thermoset prepreg cures*. *Journal of Applied Polymer Science*, 50(9):1555–1564, 1993.
- [49] NAWAB, YASIR, XAVIER TARDIF, NICOLAS BOYARD, VINCENT SOBOTKA, PASCAL CASARI FRÉDÉRIC JACQUEMIN: *Determination and Modeling of the cure shrinkage of epoxy vinylester resin and associated composites by considering thermal gradients*. *Composites Science and Technology*, 73, 10 2012.
- [50] NEUNKIRCHEN, STEFAN RALF SCHLEDJEWSKI: *Tack measurement of bindered rovings for the dry fiber winding process*. *Polymer Composites*, 42(9):4607–4616, 2021.
- [51] OPALIČKI, M., J. M. KENNY L. NICOLAIS: *Cure kinetics of neat and carbon-fiber-reinforced TGDDM/DDS epoxy systems*. *Journal of Applied Polymer Sci-*

- ence, 61(6):1025–1037, 1996.
- [52] PARK, SOO-JIN MIN-KANG SEO: *Chapter 8 - Composite Characterization*. PARK, SOO-JIN MIN-KANG SEO (): *Interface Science and Composites*, 18 *Interface Science and Technology*, 631–738. Elsevier, 2011.
- [53] PATEL, AMMAR, ANTHONY MAIORANA, LIANG YUE, RICHARD GROSS ICA MANAS-ZLOCZOWER: *Curing Kinetics of Biobased Epoxies for Tailored Applications*. *Macromolecules*, 49, 07 2016.
- [54] POSTACCHINI, LEONARDO, MICHELA SIMONCINI, FORCELLESE ARCHIMEDE, MAURIZIO BEVILACQUA, FILIPPO EMANUELE CIARAPICA, GIUSTINIANO ANDREASSI ANNA RUSSO: *Environmental assessment of an automated impregnation process of carbon fiber tows*. *Procedia CIRP*, 88:445–450, 01 2020.
- [55] ROBERT, COLIN, TOA PECUR, JAMES M. MAGUIRE, AUSTIN D. LAFERTY, EDWARD D. MCCARTHY CONCHÚR M. Ó BRÁDAIGH: *A novel powder-epoxy towpregging line for wind and tidal turbine blades*. *Composites Part B: Engineering*, 203:108443, 2020.
- [56] RUIZ, EDU FRANCOIS TROCHU: *Thermomechanical Properties during Cure of Glass-Polyester RTM Composites: Elastic and Viscoelastic Modeling*. *Journal of Composite Materials - J COMPOS MATER*, 39:881–916, 05 2005.
- [57] SABA, N., M. JAWAID M.T.H. SULTAN: *1 - An overview of mechanical and physical testing of composite materials*. JAWAID, MOHAMMAD, MOHAMED THARIQ NAHEED SABA (): *Mechanical and Physical Testing of Biocomposites, Fibre-Reinforced Composites and Hybrid Composites*, Woodhead Publishing Series in Composites Science and Engineering, 1–12. Woodhead Publishing, 2019.
- [58] SALEHHUDIN, HANNA, EDZROL MOHAMAD, WAN MAHADI AMALINA AFIFI: *Multiple-jet electrospinning methods for nanofiber processing: A review*. *Materials and Manufacturing Processes*, 33:479–498, 10 2017.
- [59] SOUROUR, S. M.R. KAMAL: *Differential scanning calorimetry of epoxy cure: isothermal cure kinetics*. *Thermochimica Acta*, 14(1):41–59, 1976.
- [60] SUZUKI, KATSUHITO, YASUSHI MIYANO TAKESHI KUNIO: *Change of viscoelastic properties of epoxy resin in the curing process*. *Journal of Applied Polymer Science*, 21(12):3367–3379, 1977.
- [61] VAIDYA, UDAY: *Continuous Fiber Reinforcement Based Processes For Automotive, Heavy Trucks and Mass Transit*, 2011.
- [62] WANG, YI, SARTHAK MAHAPATRA, JONATHAN P.-H. BELNOUE, DMITRY S. IVANOV STEPHEN R. HALLETT: *Understanding tack behaviour during prepreg-based composites' processing*. *Composites Part A: Applied Sci-*

- ence and Manufacturing, 164:107284, 2023.
- [63] WISNOM, MICHAEL R., TOM REYNOLDS NIGEL GWILLIAM: *Reduction in interlaminar shear strength by discrete and distributed voids*. Composites Science and Technology, 56(1):93–101, 1996.
- [64] WU, FENG, XINGPING ZHOU XINHAI YU: *Reaction mechanism, cure behavior and properties of a multifunctional epoxy resin, TGDDM, with latent curing agent dicyandiamide*. RSC Adv., 8:8248–8258, 2018.
- [65] ZHAO, DA, TAO LIU, MEI ZHANG, RICHARD LIANG BEN WANG: *Fabrication and characterization of aerosol-jet printed strain sensors for multifunctional composite structures*. Smart Materials and Structures, 21(11):115008, sep 2012.
- [66] ÇELİK, MURAT, THOMAS NOBLE, FRANK JORGE, RONGQING JIAN, CONCHUR O’BRADAIGH COLIN ROBERT: *Influence of Line Processing Parameters on Properties of Carbon Fibre Epoxy Towpreg*. Journal of Composites Science, 03 2022.

List of Figures

1.1	Schematic diagram of the wet winding process [38]	1
1.2	Towpreg winding. Retrieved from TCR Composites	1
1.3	LCC's towpreg machine	2
2.1	Schematic diagram of the towpreg machine's stages	4
2.2	Dry fiber spools unwinding section	4
2.3	Impregnation unit	5
2.4	Fulling rollers	6
2.5	New guide rollers	7
2.6	Thermocouples attached to first fulling roller's surface	8
2.7	Fulling roller surface abrasion	8
2.8	Thermocouples measurements	8
2.9	Cooling unit	9
2.10	Cross-winders	9
2.11	Parallel-winder	9
2.12	Fiber damage on a cross-winder roller	10
2.13	ILSS test setup	11
2.14	Curved beam bending test setup	11
3.1	Setup of the vacuum bagging of the plates	20
3.2	Sealed plate in the press	20
3.3	Cured plate	21
3.4	Plates after cutting	21
3.5	Setup of the vacuum bagging of the cylinders	21
3.6	Finished cylinder	21
3.7	ILSS test sample	22
3.8	ILSS test setup	22
3.9	Curved beam bending test sample	23
3.10	Curved beam bending test setup	23
3.11	Porosity analysis of a sample from the 100°C_NEW plate	24
3.12	FVC analysis of a sample from the 100°C_NEW plate	24
3.13	Heat flow vs temperature curve from a DSC dynamic measurement on the Huntsman resin	25
3.14	Heat flow vs time curve from a DSC isothermal measurement (140°C) on the Huntsman resin	25
3.15	$G(\alpha)$ curves from linear fitting of $K(T)$	29
3.16	$G(\alpha)$ curves from quadratic fitting of $K(T)$	29

4.1	ILSS test results	31
4.2	Accepted failure modes by the standards [3]	32
4.3	Rejected failure modes by the standards [3]	32
4.4	Failure mode from testing (span = 10 mm)	33
4.5	Force-displacement graph of a 60°C_NEW sample (span = 10 mm)	33
4.6	Average tow temperatures after calender	33
4.7	Viscosity of Huntsman resin system	33
4.8	Curved beam bending strength	34
4.9	Curved beam bending modulus	35
4.10	Compressive and delamination failure	35
4.11	Curved beam bending force-deflection graph	35
4.12	Porosity analysis results	36
4.13	FVC analysis results	37
4.14	100°C_OLD micrograph at 5x magnification	38
4.15	100°C_NEW micrograph with 5.78% porosity	38
4.16	80°C_NEW micrograph with 8.01% porosity	38
4.17	Huntsman $d\alpha/dt$ vs t from experimental results	39
4.18	Huntsman α vs t from experimental results	39
4.19	Hexion $d\alpha/dt$ vs t from experimental results	40
4.20	Hexion α vs t from experimental results	40
4.21	Experimental vs Kamal & Sourour's model predicted DoC for the Huntsman system	42
4.22	Experimental vs Kamal & Sourour's model predicted DoC for the Hexion system	42
4.23	Experimental vs Bailleul's model predicted DoC for the Huntsman system	43
4.24	Experimental vs Bailleul's model predicted DoC for the Hexion system	44
4.25	Experimental $G(\alpha)$ function against the $G(\alpha)$ function of the model of Hexion	44

List of Tables

3.1	Resin systems used in the investigation	17
3.2	Fiber and resin data	19
3.3	Towpregs used in the investigation	19
3.4	DSC dynamic rscan segments	26
3.5	DSC isothermal scan segments	26
3.6	Isothermal temperatures selected for the DSC scans	27
3.7	Probe tack test parameters	30
3.8	Probe tack test setup	30
4.1	Results of the DSC dynamic scans	39
4.2	Kamal & Sourour's model parameters summary	41
4.3	Bailleul's model parameters summary	43
4.4	Results of the 4 probe tack tests	45
1	ILSS test samples dimensions and results (part 1)	58
2	ILSS test samples dimensions and results (part 2)	59
3	Curved beam bending test samples dimensions and results	60

Appendix

Table 1 : ILSS test samples dimensions and results (part 1)

Plate	Sample No.	b[mm]	h[mm]	Lv[mm]	Fmax[N]	Stress [MPa]
40°C_OLD	1	7,75	1,58	10	748,86	45,87
40°C_OLD	2	7,95	1,56	10	766,8	46,37
40°C_OLD	3	7,93	1,6	10	712,78	42,13
40°C_OLD	4	7,9	1,57	10	784,68	47,45
40°C_OLD	5	7,96	1,59	10	756,91	44,85
40°C_OLD	6	7,87	1,59	10	794,13	47,60
40°C_OLD	7	7,88	1,56	10	806,57	49,21
40°C_OLD	8	7,98	1,57	10	745,51	44,63
40°C_OLD	9	7,85	1,57	10	786,2	47,84
40°C_OLD	10	8,09	1,6	10	1059,88	61,41
100°C_OLD	1	8,17	1,6	10	1015,45	58,26
100°C_OLD	2	7,9	1,6	10	992,47	58,89
100°C_OLD	3	8,01	1,6	10	942	55,13
100°C_OLD	4	8,15	1,62	10	1027,31	58,36
100°C_OLD	5	7,99	1,61	10	1033,48	60,25
100°C_OLD	6	8,03	1,61	10	939,55	54,51
100°C_OLD	7	7,96	1,63	10	1023,43	59,16
100°C_OLD	8	8,05	1,63	10	1002,84	57,32
100°C_OLD	9	8,14	1,61	10	981,02	56,14
100°C_OLD	10	7,9	1,59	10	1026,43	61,29
40°C_NEW	1	7,77	1,59	10	848,3	51,50
40°C_NEW	2	7,77	1,58	10	776,68	47,45
40°C_NEW	3	7,82	1,6	10	903,4	54,15
40°C_NEW	4	7,9	1,6	10	696,04	41,30
40°C_NEW	5	7,91	1,58	10	938,93	56,35
40°C_NEW	6	7,81	1,57	10	841,44	51,47
40°C_NEW	7	7,87	1,57	10	852,88	51,77
40°C_NEW	8	7,93	1,59	10	817,86	48,65
40°C_NEW	9	7,86	1,65	10	919,92	53,20
40°C_NEW	10	7,94	1,62	10	1329,22	77,50

Table 2 : ILSS test samples dimensions and results (part 2)

Plate	Sample No.	b[mm]	h[mm]	Lv[mm]	Fmax[N]	Stress[MPa]
100°C_NEW	1	7,91	1,55	10	912,2	55,80
100°C_NEW	2	7,78	1,55	10	874,75	54,40
100°C_NEW	3	7,79	1,59	10	907,6	54,96
100°C_NEW	4	7,91	1,59	10	838,95	50,03
100°C_NEW	5	7,76	1,58	10	841,42	51,47
100°C_NEW	6	7,83	1,57	10	877,36	53,53
100°C_NEW	7	7,78	1,53	10	826,64	52,08
100°C_NEW	8	7,83	1,54	10	861,51	53,58
100°C_NEW	9	7,77	1,55	10	876,7	54,60
100°C_NEW	10	7,9	1,57	10	869,17	52,56
MITSU	1	7,54	1,47	10	1090,66	73,80
MITSU	2	7,48	1,49	10	1049,22	70,61
MITSU	3	7,6	1,55	10	997,71	63,52
MITSU	4	7,47	1,5	10	965,01	64,59
MITSU	5	7,41	1,53	10	981,46	64,93
MITSU	6	7,44	1,47	10	973,09	66,73
MITSU	7	7,46	1,52	10	956,68	63,28
MITSU	8	7,5	1,531	10	1033,34	67,49
MITSU	9	7,55	1,53	10	1000,67	64,97
MITSU	10	7,3	1,52	10	1000,46	67,62
80°C_NEW	1	8,05	1,47	10	875,61	55,50
80°C_NEW	2	7,75	1,63	10	911,2	54,10
80°C_NEW	3	7,56	1,56	10	953,77	60,65
80°C_NEW	4	7,86	1,49	10	803,35	51,45
80°C_NEW	5	7,79	1,54	10	830,45	51,92
80°C_NEW	6	7,76	1,5	10	904,2	58,26
80°C_NEW	7	7,68	1,49	10	925,75	60,67
80°C_NEW	8	7,74	1,54	10	807,74	50,82
80°C_NEW	9	7,78	1,55	10	828,66	51,54
80°C_NEW	10	7,53	1,52	10	783,79	51,36
60°C_NEW	1	7,89	1,5	10	819,76	51,95
60°C_NEW	2	7,72	1,57	10	826,68	51,15
60°C_NEW	3	7,49	1,51	10	766,7	50,84
60°C_NEW	4	7,98	1,56	10	860,27	51,83
60°C_NEW	5	7,9	1,47	10	914,09	59,03
60°C_NEW	6	7,63	1,52	10	912,54	59,01
60°C_NEW	7	7,76	1,53	10	809,63	51,14
60°C_NEW	8	7,96	1,58	10	856,38	51,07
60°C_NEW	9	7,98	1,58	10	859,01	51,10
60°C_NEW	10	7,57	1,54	10	886,71	57,05

Table 3 : Curved beam bending test samples dimensions and results

Cylinder	Sample No.	b[mm]	h[mm]	L _v [mm]	F _{max} [N]
50°C_OLD	1	15,15	1,45	60	509,97
50°C_OLD	2	15,39	1,46	60	474,73
50°C_OLD	3	15,37	1,45	60	487,83
50°C_OLD	4	15,32	1,46	60	507,16
50°C_OLD	5	15,42	1,44	60	435,75
MITSU	1	15,5	1,4	60	486,71
MITSU	2	15,55	1,4	60	481,24
MITSU	3	15,23	1,43	60	477,55
MITSU	4	15,3	1,45	60	490,9
MITSU	5	15,26	1,45	60	452,15
60°C_NEW	1	15,52	1,42	54	486,2
60°C_NEW	2	14,9	1,39	54	504,71
60°C_NEW	3	15,42	1,39	54	503,25
60°C_NEW	4	15,49	1,38	54	509,95
60°C_NEW	5	15,44	1,39	54	540,13
100°C_NEW	1	15,51	1,47	58	471,25
100°C_NEW	2	15,43	1,45	58	527,53
100°C_NEW	3	15,47	1,52	58	496,51
100°C_NEW	4	15,45	1,45	58	497,16
100°C_NEW	5	15,44	1,5	58	477,69